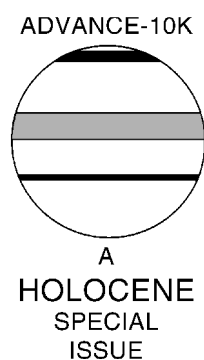


# Tree-ring width and density data around the Northern Hemisphere: Part 2, spatio-temporal variability and associated climate patterns

Keith R. Briffa,<sup>1\*</sup> Timothy J. Osborn,<sup>1</sup> Fritz H. Schweingruber,<sup>2</sup> Philip D. Jones,<sup>1</sup> Stepan G. Shiyatov<sup>3</sup> and Eugene A. Vaganov<sup>4</sup>

(<sup>1</sup>*Climatic Research Unit, University of East Anglia, Norwich NR4 7TJ, UK;* <sup>2</sup>*Swiss Federal Institute of Forest, Snow and Landscape Research, Zurcherstrasse 111, CH-8903, Birmensdorf, Switzerland;* <sup>3</sup>*Institute of Plant and Animal Ecology, Ural Division of the Russian Academy of Sciences, 8 Marta Street 202, Ekaterinburg 620219, Russia;* <sup>4</sup>*Institute of Forest, Siberian Division of the Russian Academy of Sciences, Akagemgorodok, Krasnoyarsk 660036, Russia)*



**Abstract:** Patterns of summer temperature over the Northern Hemisphere, obtained from a calibration of a tree-ring network, are presented for every year from 1600 to 1877. The network of tree-ring density chronologies is shown to exhibit spatially coherent modes of variability. These modes closely match summer half-year temperature variations, in terms of similar spatial patterns and similar temporal evolution during the instrumental period. They can, therefore, be considered to be proxies for the temperature patterns, and time series for the eight most dominant patterns are presented back to the late seventeenth century. The first pattern represents spatially coherent warming or cooling and it appears to respond to climate forcings, especially volcanic eruptions. Most other patterns appear to be related to atmospheric pressure anomalies and they can be partially explained by heat advection associated with anomalous atmospheric circulation. This provides the potential for reconstructing past variations in atmospheric circulation for the summer half-year. To investigate this potential, modes of summer-pressure variability are defined, and an attempt is made to reconstruct them using principal components regression. Poor verification statistics and high sensitivity to the design of the regression procedure provide little confidence in the reconstructions presented, which are regarded as being preliminary only. A repeat study using instrumental temperature predictors shows that the poor performance is attributable mainly to the weakness of the relationship between air temperature over land and atmospheric circulation during summer: though a relationship exists, it is not strong enough to yield reliable regression models when only a relatively short overlap period (55 years in this study) exists for calibration and verification. Further attempts to reconstruct large-scale atmospheric circulation patterns that include precipitation-sensitive networks of tree-ring data are likely to produce improved results.

**Key words:** Dendroclimatology, tree-ring density, regional climate, summer-temperature patterns, circulation modes, Northern Hemisphere, late Holocene.

## Introduction

Briffa *et al.*, Part 1 (this issue; henceforth referred to as Part 1), present a detailed review of the statistical associations between

interannual tree growth (ring width and maximum latewood density) and observed temperature and precipitation variability, both at individual sites across a large network and for a range of large regional-scale chronology averages. Although there are a number of climate signals recorded within the network, it is demonstrated in Part 1 that the dominant growth-forcing signal is

\*Author for correspondence (e-mail: k.briffa@uea.ac.uk)

that of 'warm-season' temperature and that the Maximum Latewood Density (MXD) data exhibit a stronger expression of thermal forcing on interannual to multidecadal timescales and hence possess a greater potential for the reconstruction of past high-frequency temperature variability than is the case for the tree-ring-width data (particularly at the scale of individual sites). The standardization that has been applied to the tree-ring chronologies suppresses the intercentennial variability (Cook *et al.*, 1995; Briffa *et al.*, 1996); to be compatible with Part 1, we have *not* used the method of Briffa *et al.* (2001) that preserves low-frequency variations.

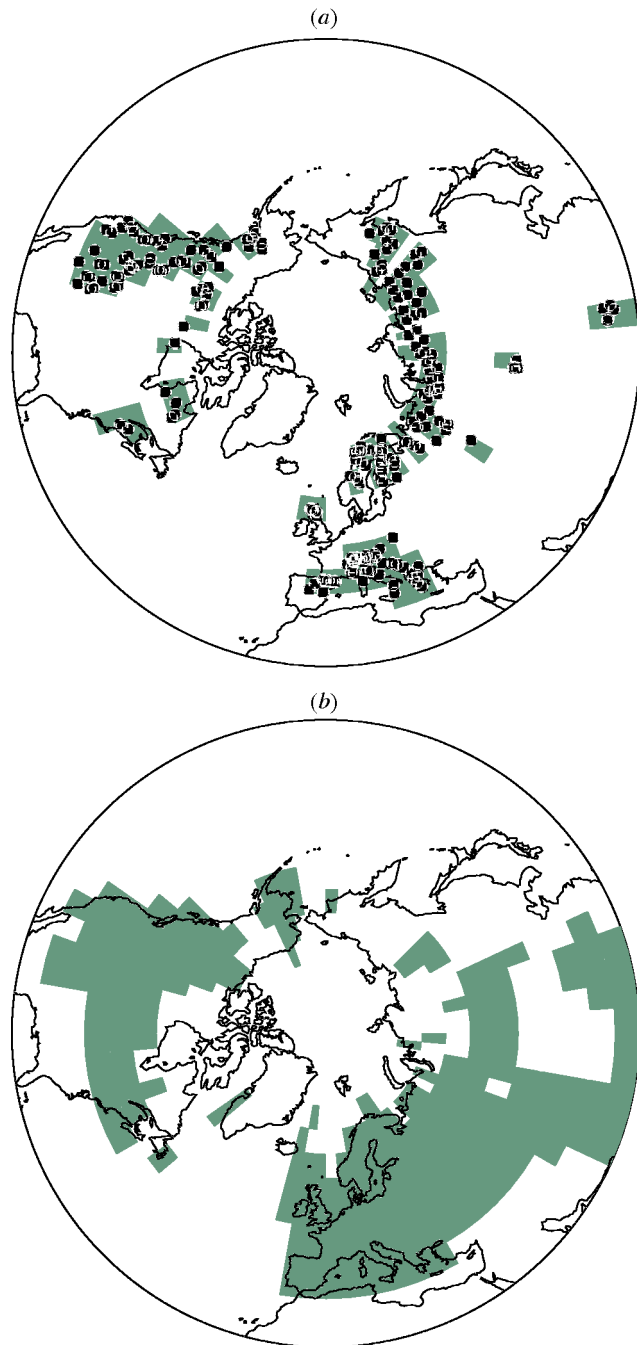


**Figure 1** (a) Location (circles) of the 303 sites with tree-ring density chronologies that correlate significantly with their local grid-box growing-season (April–September mean) temperature and that fall in one of the 92 5° latitude by 5° longitude grid boxes (grey shading) that have at least one chronology with data back to 1697. (b) Grey shading indicates those grid boxes with almost complete instrumental land temperature data for 1922–98 and are used in attempts to reconstruct summer-circulation patterns as a basis for comparing the skill of the tree-ring density predictors.

Our purpose in the current paper is to identify the leading spatio-temporal modes of variability evident in the MXD data and to associate these with patterns of growing-season temperature variability. We then consider why particular modes of temperature variability occur. Specific mechanisms must be responsible for these modes to recur in a similar way over a period of time, such as the operation of some external forcing agent or the recurrence of some characteristic pattern in the organization of oceanic or atmospheric circulation. It is difficult, however, to separate characteristic modes using short records, so the MXD data set provides an opportunity to attempt this, using a record that is much longer than the period with good instrumental coverage. Briffa *et al.* (1998a) have already identified the cooling signal of explosive volcanic eruptions in the MXD data set. Here, we focus on the link between summer atmospheric circulation and surface temperature in an attempt to explain the patterns of summer temperature variability identified in the MXD data set. The link between circulation and temperature is much weaker in summer than in winter, because the summer atmospheric circulation is less well organized into recurrent large-scale modes (Wallace and Gutzler, 1981; Barnston and Livezey, 1987) and also exerts less control over surface temperature (see, for example, Osborn *et al.*, 1999). Nevertheless, we explore the potential for producing reconstructions of the most important Northern Hemisphere atmospheric circulation modes.

We first provide details of tree-ring MXD and the various climate data sets used for these analyses. The dominant modes of MXD variability and associated temperature and precipitation relationships are then presented and discussed, and results of attempts to reconstruct the variability of atmospheric circulation modes using the MXD in previous centuries are described.

## Tree-ring and instrumental climatic data

### Tree-ring density data

The Maximum Latewood Density (MXD) set with which we begin these analyses comprises data at 387 high-latitude or high-elevation locations (see Figure 1 of Part 1; Schweingruber and Briffa, 1996). The dominant climate signal in the MXD network is identified in Part 1 as the April–September temperature mean. Following Part 1, 46 chronologies that do not exhibit significant correlations with their local grid-box temperatures over this seasonal window were discarded, leaving 341 chronologies. These chronologies have been interpolated onto a regular grid and calibrated with reference to modern temperature observations to produce a continuous year-by-year set of past growing-season temperature maps. We present only a brief summary of the approach in a later section as full details will be provided elsewhere (Osborn *et al.*, 2002).

As in Part 1, the tree-ring chronologies have been standardized (to remove the non-climatic influence of tree age), but this also results in a loss of the low-frequency climate signal (Cook *et al.*, 1995; Briffa *et al.*, 1996). Briffa *et al.* (2001) used an alternative method (age band decomposition) to preserve this signal and demonstrated that the standardized data used here are likely to have lost some variance at periods longer than 30 years, though it is only at periods longer than 100 years that a large difference is evident. These data are not used here because Briffa *et al.* (2001) only applied their technique at the regional-average scale. Thus, any intercentennial variability in the reconstructions presented here will have been, at least partly, suppressed.

### Climatic data

Four sets of instrumental data are used in this study, two for temperature and two for sea-level pressure (SLP). The first set of instrumental surface temperatures for the Northern Hemisphere is

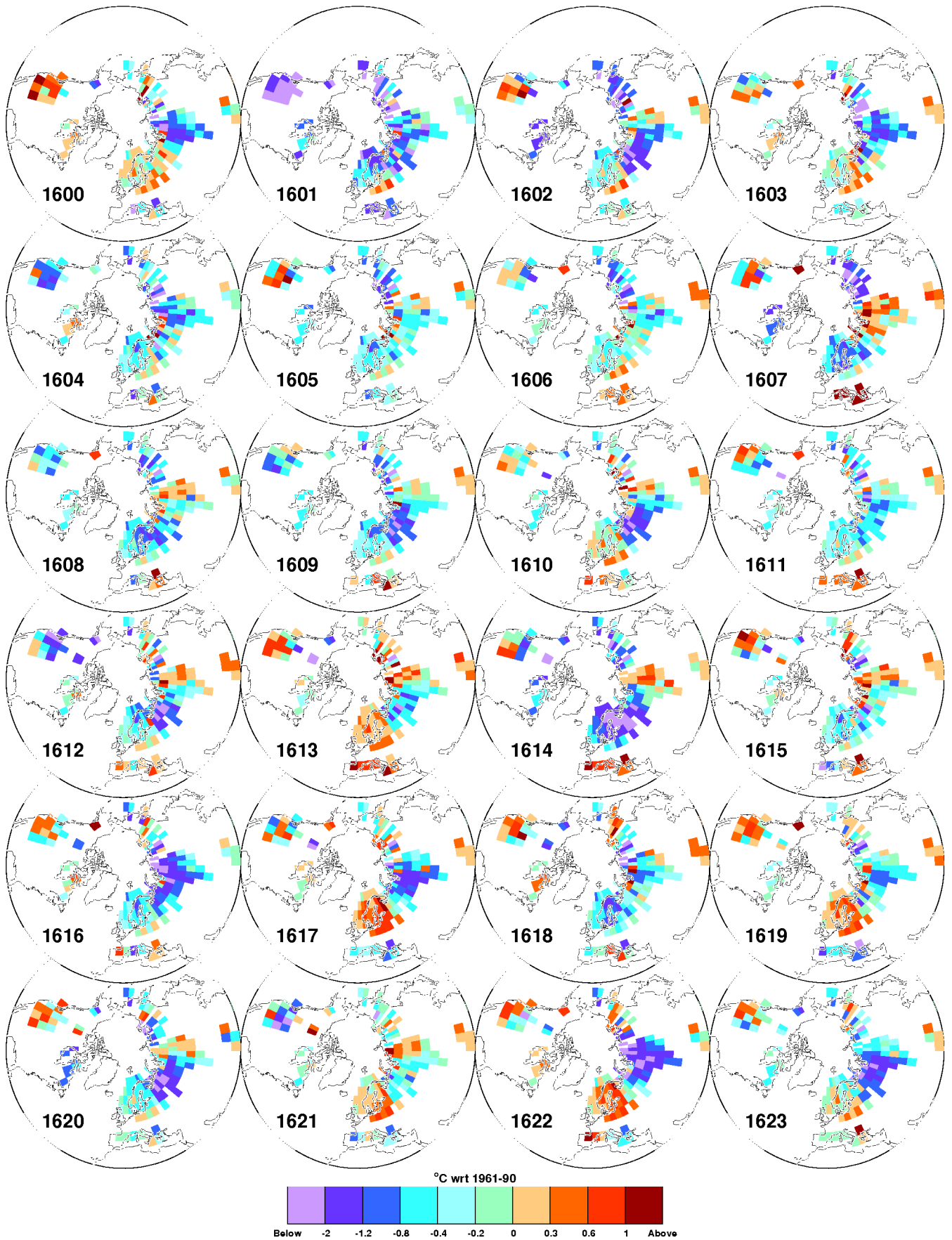


**Figure 2** Maps of estimated April–September mean temperature ( $^{\circ}\text{C}$  anomalies from the 1961–90 mean) for each year between 1600 and 1887. The method of calibration is fully described in Osborn *et al.* (2002). Individual grid-box anomalies have greater associated uncertainty than large-scale coherent regional anomalies.

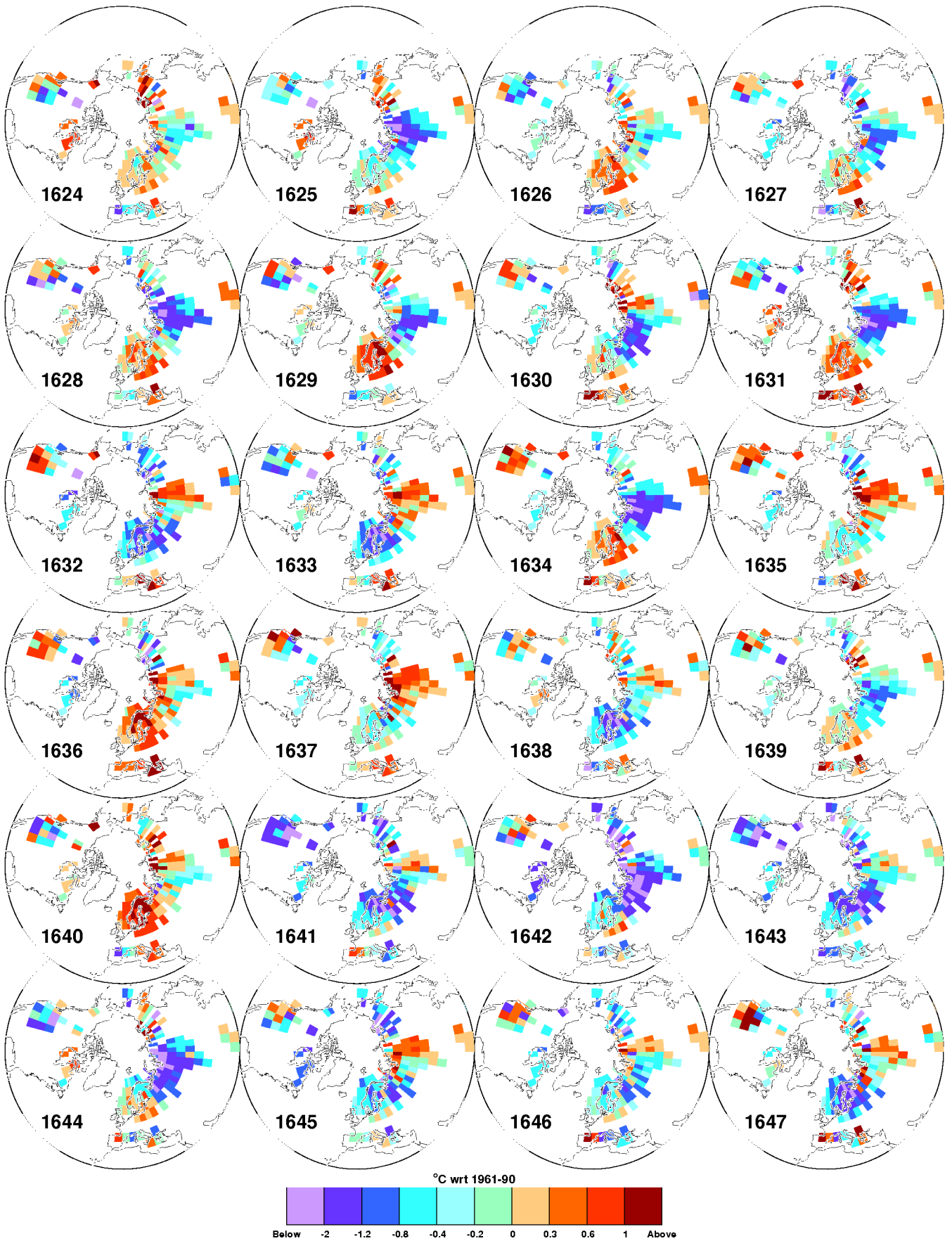


Figure 2 Continued.

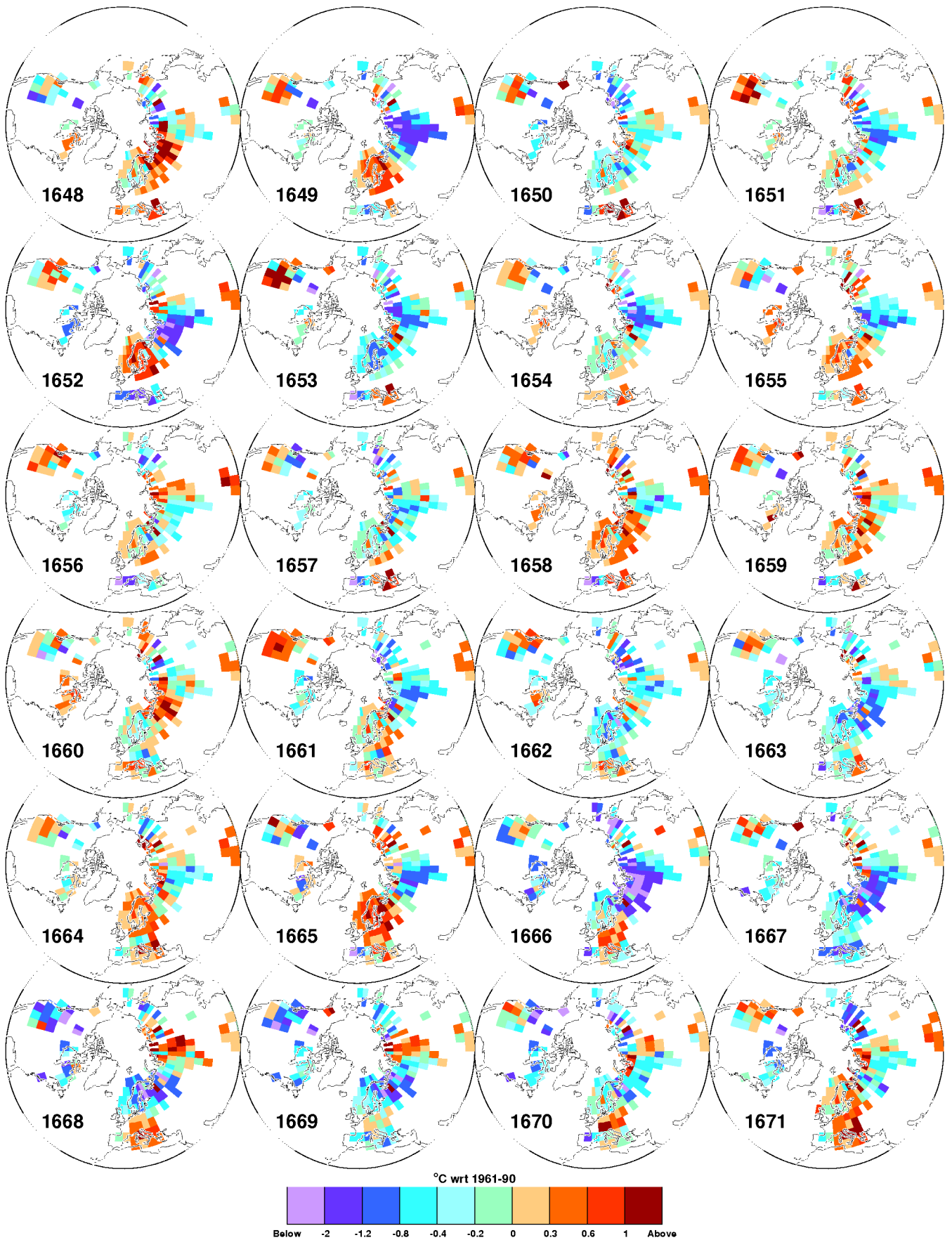


Figure 2 Continued.

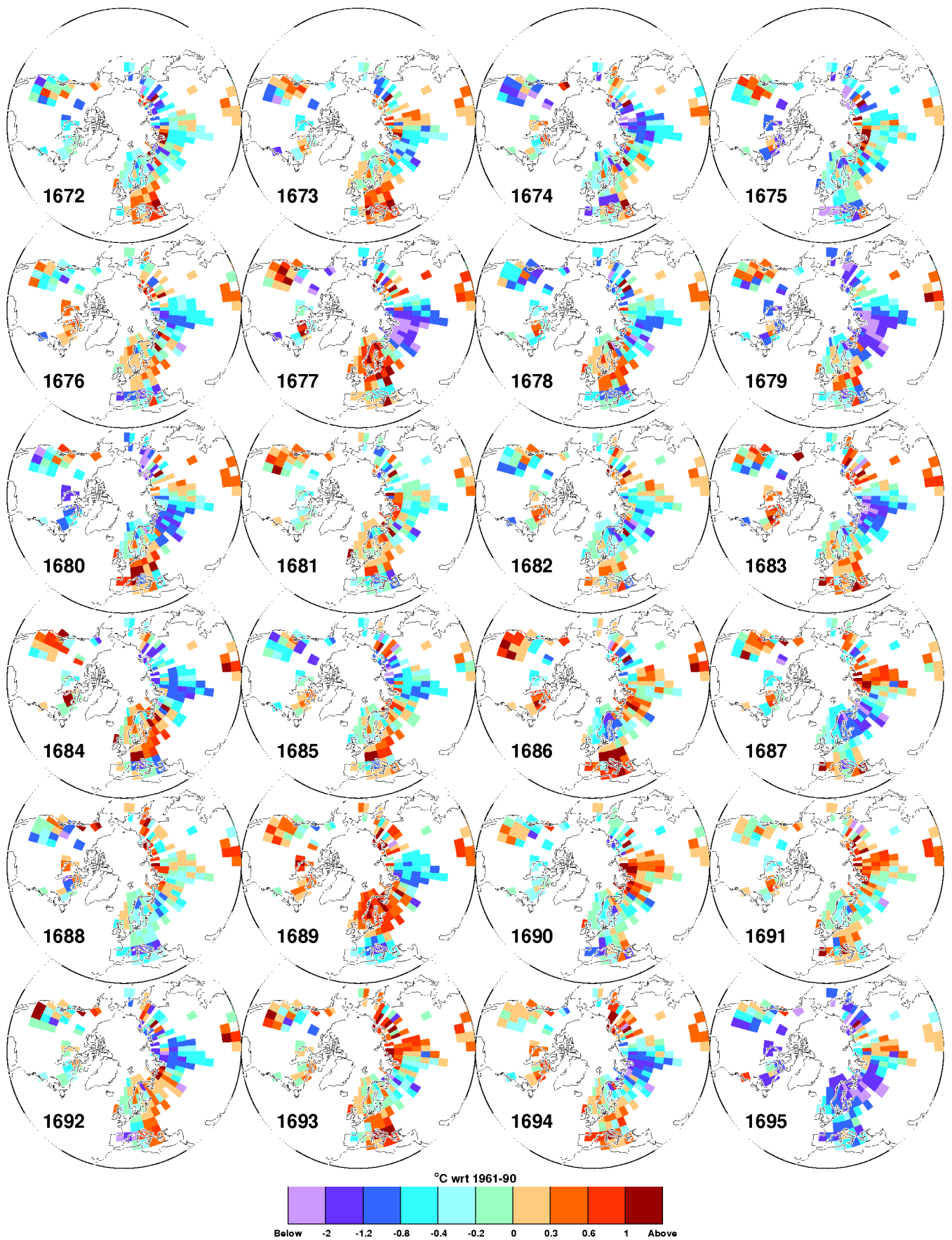


Figure 2 Continued.

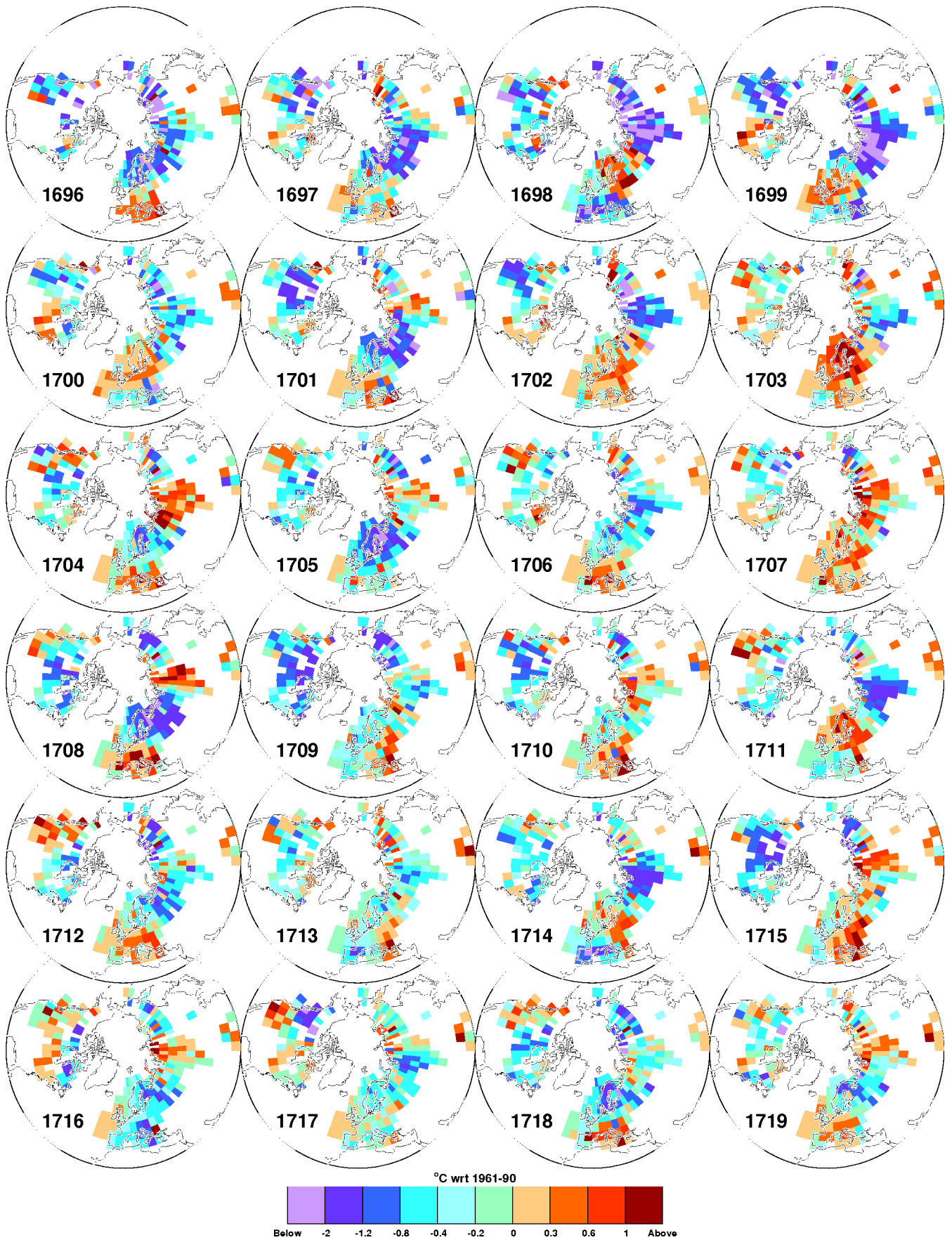


Figure 2 Continued.

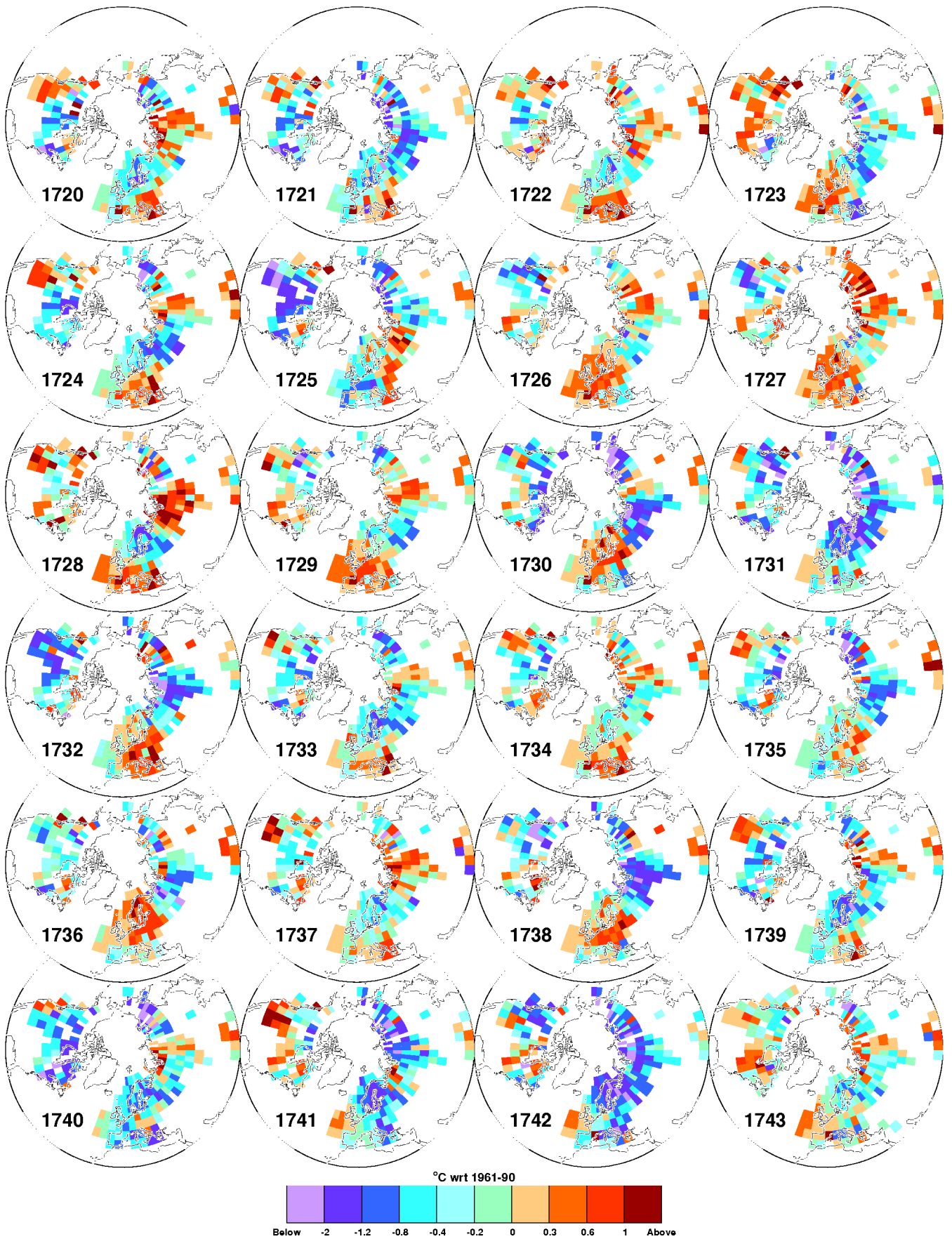


Figure 2 Continued.

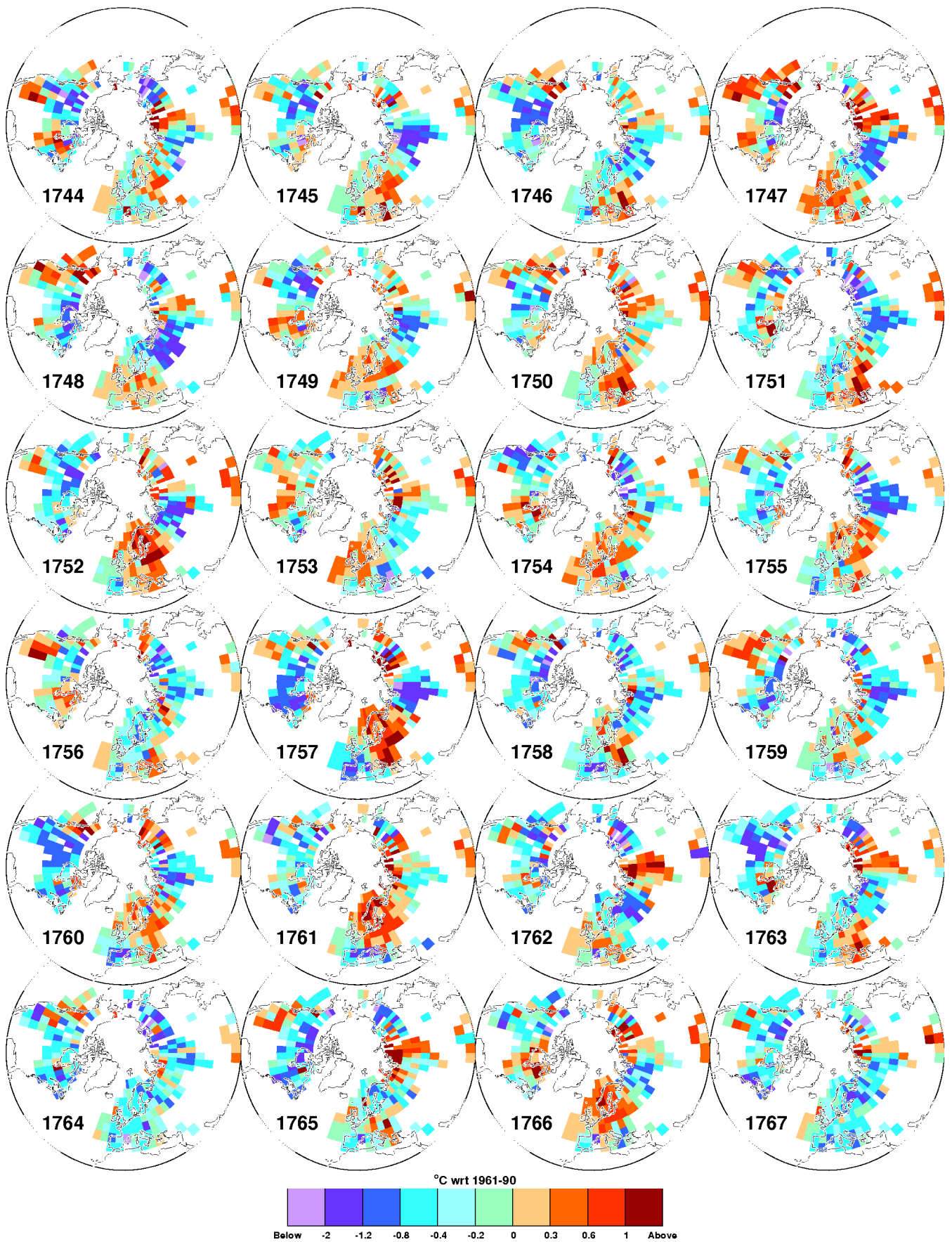


Figure 2 Continued.

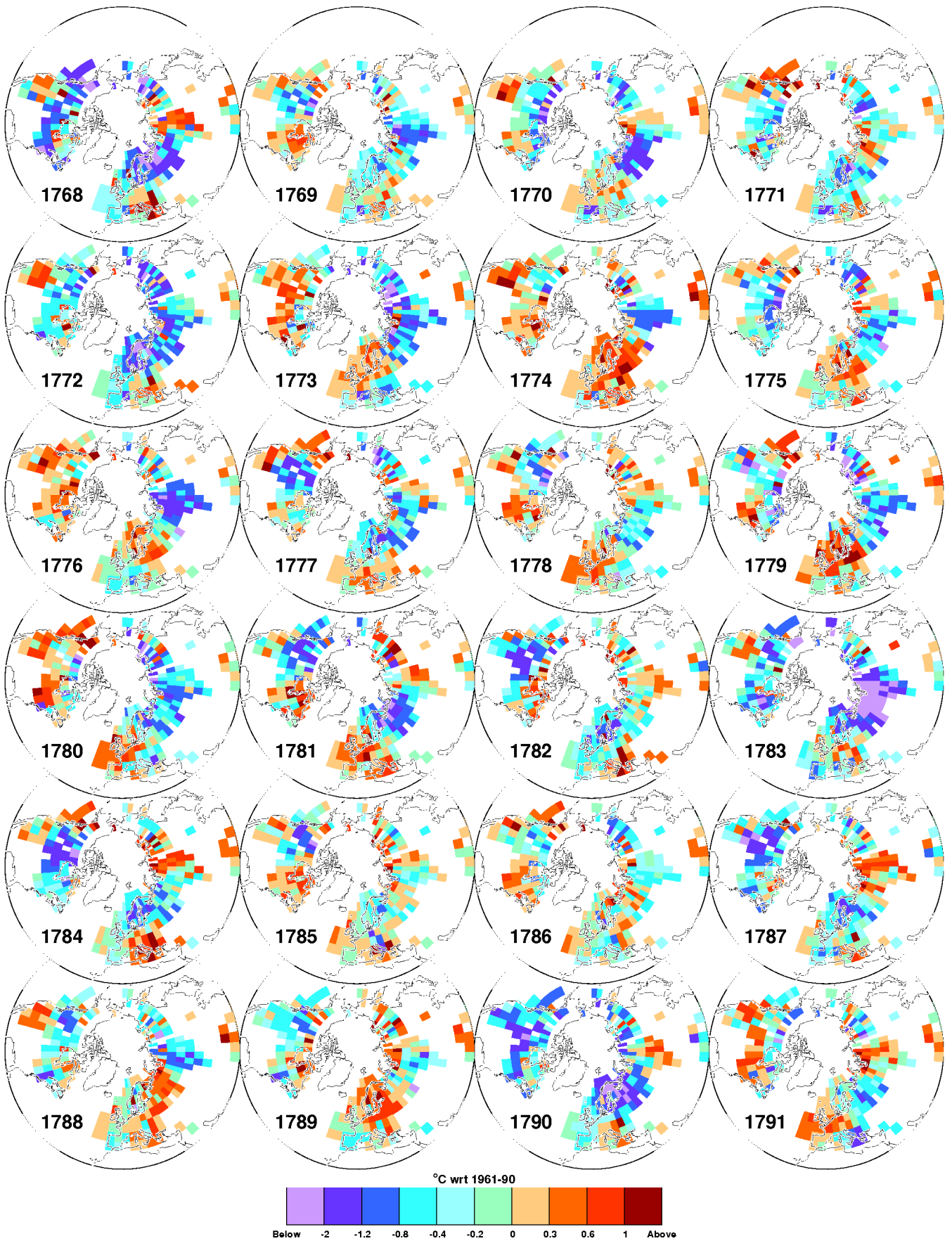


Figure 2 Continued.

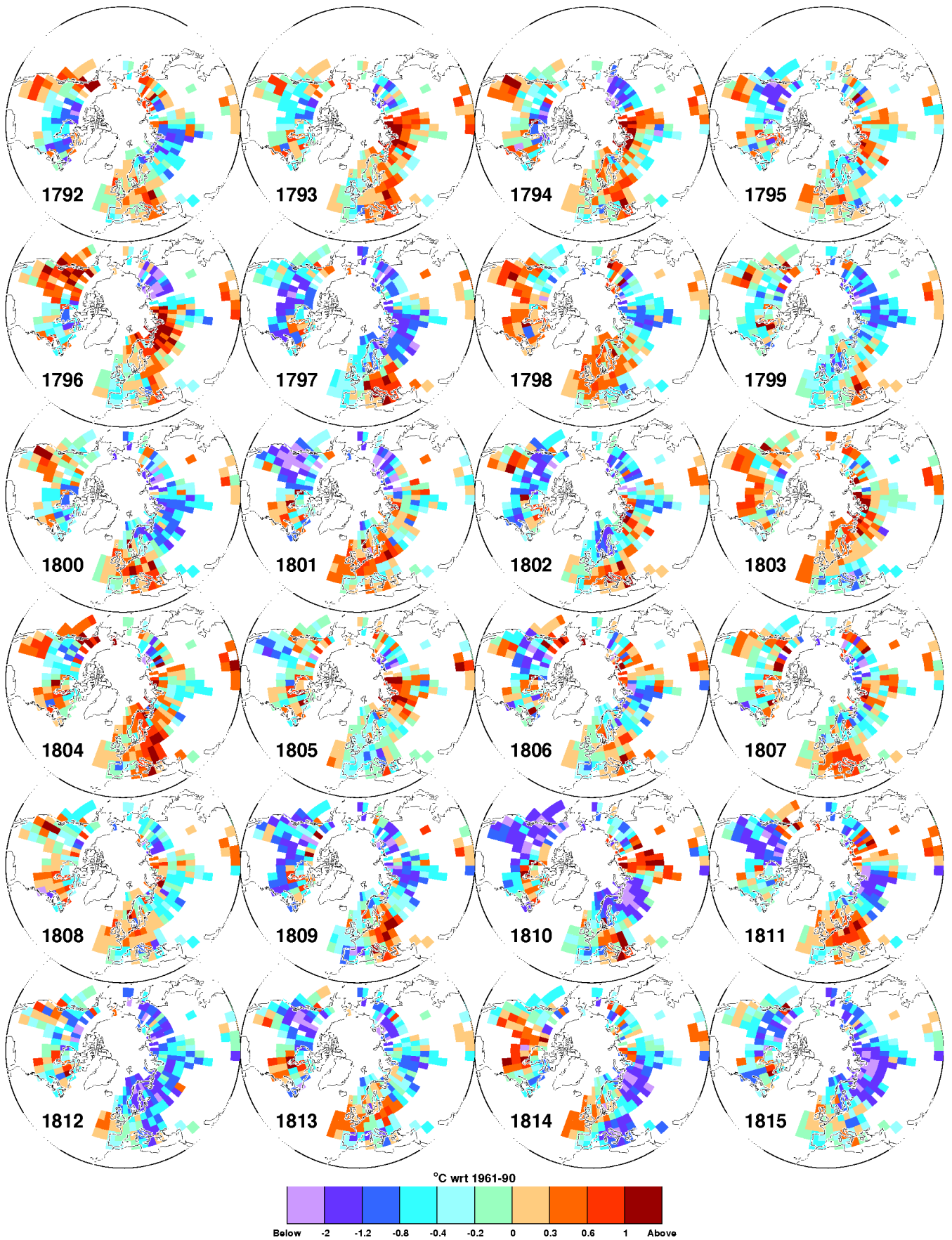


Figure 2 Continued.

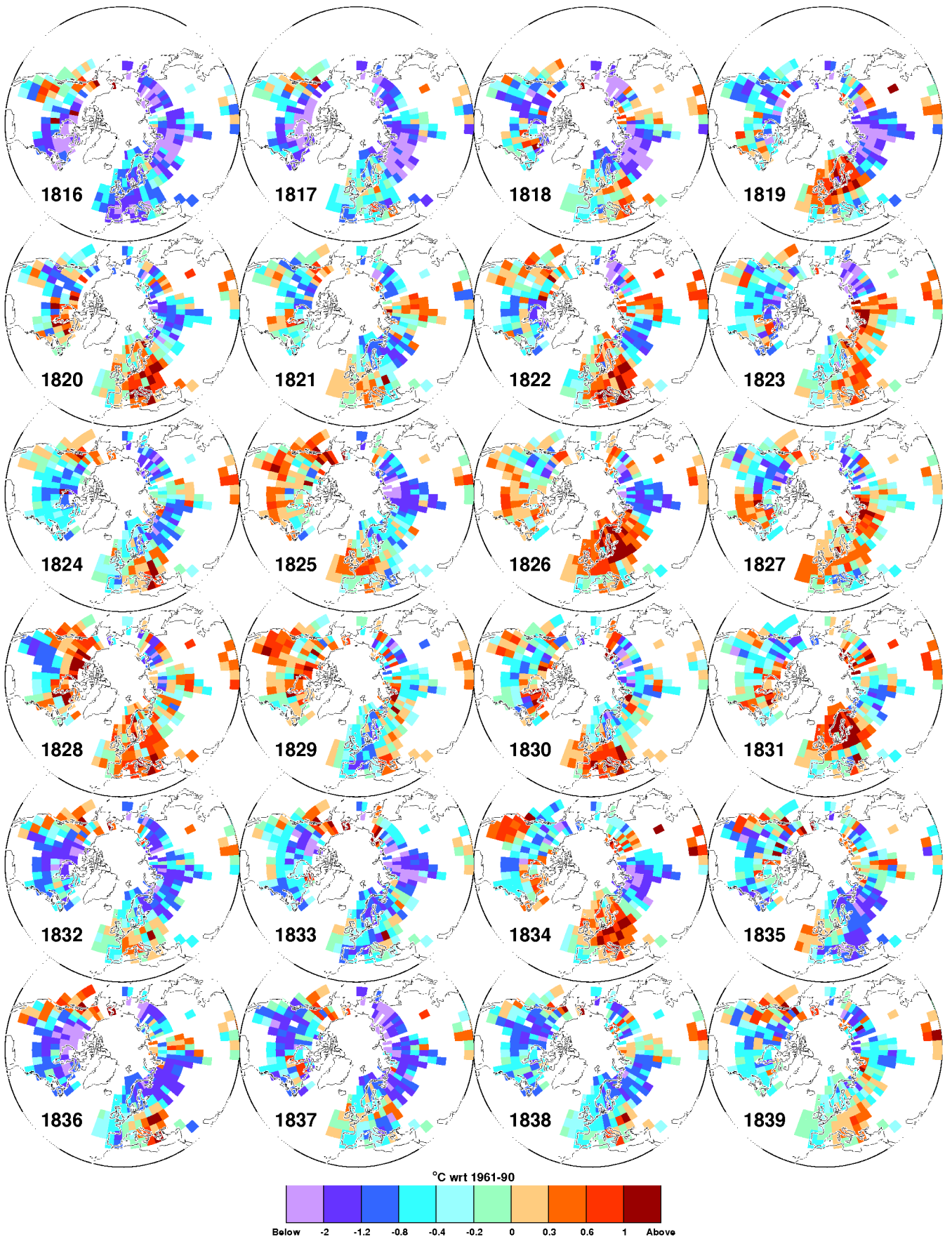


Figure 2 Continued.

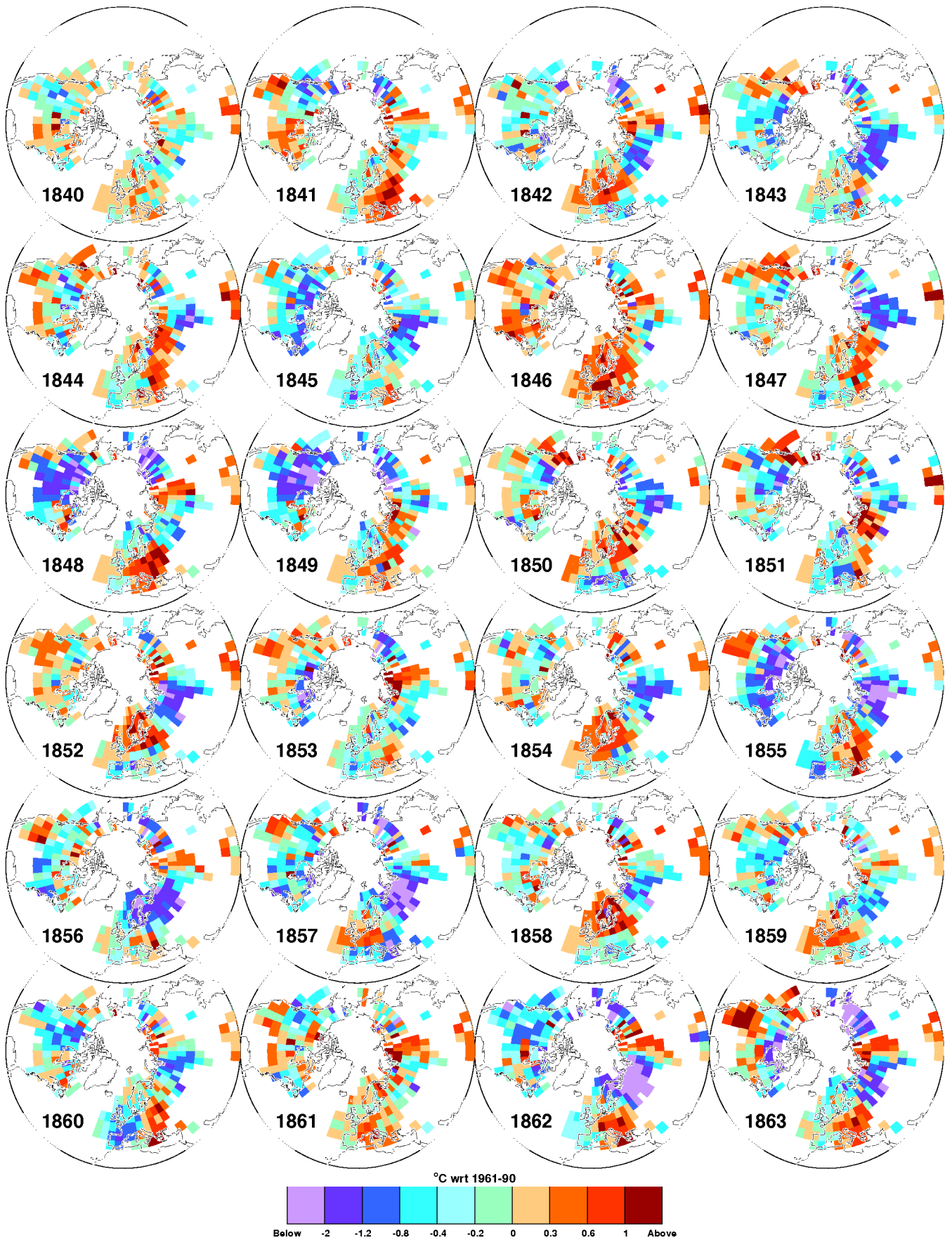


Figure 2 Continued.

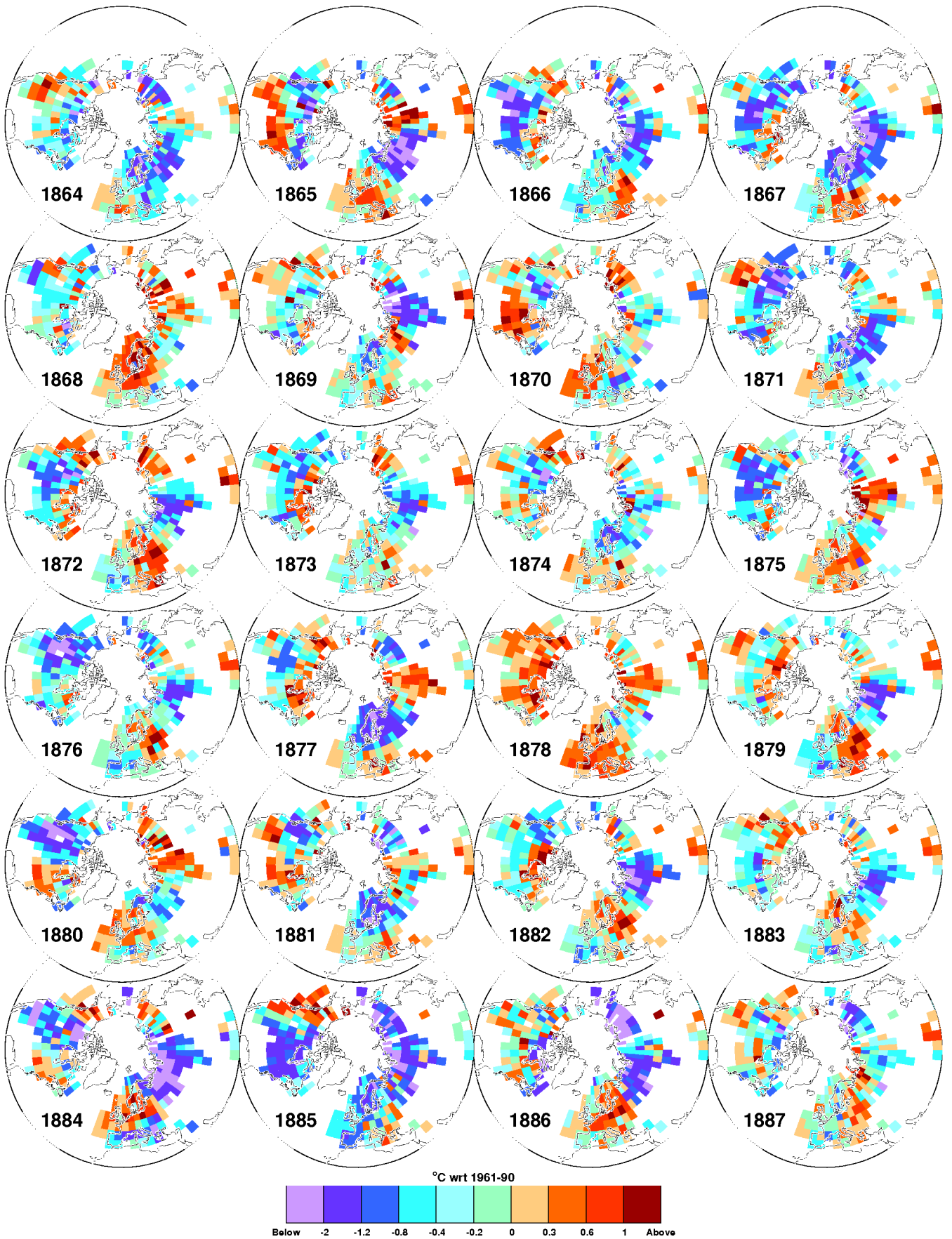
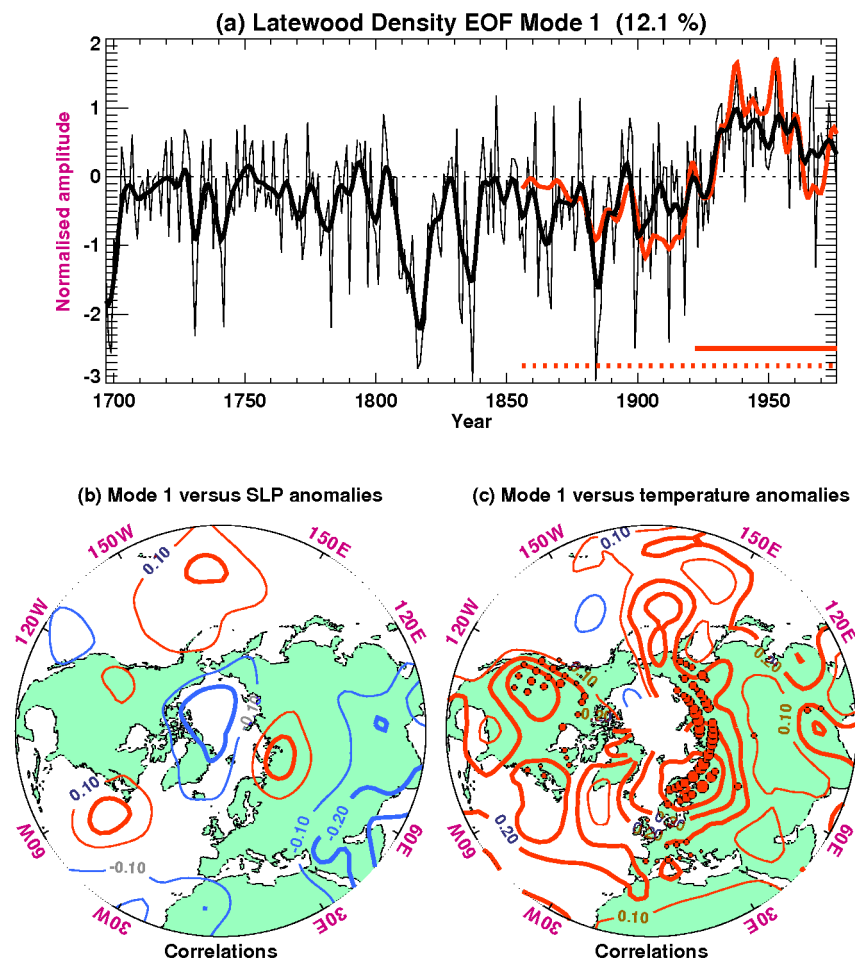


Figure 2 Continued.



**Figure 3** The first PC of the MXD data, computed from the correlation matrix calculated for the period 1697–1976. (a) PC amplitude time series (black) with decadal smoothed values (thick). (b) Correlations between the PC amplitude time series and growing-season SLP, over 1922–76 (period indicated by solid red horizontal line in (a)). (c) Contours show correlations between the PC time series and local grid-box April–September temperature, computed using all available data over 1856–1976 (period indicated by dotted red horizontal line in (a)). Dots show the PC loadings (radius proportional to loading magnitude) on the MXD data set (red positive; blue negative). Contour interval in (b) and (c) is 0.1; zero contour omitted. Also shown in (a) is the decadal smoothed time series associated with the temperature pattern indicated by the contours in (c) – see text for more details.

a combined land and marine data set (Jones *et al.*, 1999) made up of sea surface temperature anomalies (Parker *et al.*, 1995) and 1.5 m air-temperature anomalies over the land (Jones, 1994). Mean April–September temperature anomalies were calculated from each grid-box time series for whatever period was available; some have values back to the beginning of the blended data set (1856).

The land-only air temperature anomalies updated from Jones (1994) constitute the second temperature data set. These data are used here to assess the potential for reconstructing atmospheric circulation modes using only information representing land regions in summer (i.e., comparable to the tree-ring data). Again, April–September mean temperature anomalies are calculated over the Northern Hemisphere, for the period covered by the main pressure (GMSLP) data used here (1922 to 1998). To maximize the spatio-temporal coverage, April–September means were calculated if anomalies for at least three of the six months were available, and any land grid boxes that did not have an April–September value, but were surrounded by three or more land grid boxes that did, were infilled with the mean of the surrounding anomalies.

The two monthly SLP data sets are, first, an updated version of that described by Jones (1987) based mainly on UK Met Office (UKMO) synoptic charts, and, second, version 3.2 of the GMSLP data set (improved from the version described by Basnett and Parker, 1997). To ensure that results are not biased by inhomogeneities during the early period (Jones, 1987; Rogers, 1990), pre-1922 data were not used. For the UKMO data set, all values south of 20°N or poleward of 75°N were discarded; and, prior to 1950, all data from 110°E round (in an eastward direction) to 60°W at the latitudes of 70°N and 75°N were also discarded (for reasons given by Jones, 1987). Despite this removal of suspect data, our analysis (described later) strongly suggests the existence of remaining errors in the UKMO data set, so we used the GMSLP data set, for the period 1922–98, to characterize the major patterns of large-scale SLP. These latter data are available on a 5° latitude by 5° longitude grid, and mean SLP for each April–September season was computed for each grid point from the individual monthly means. To avoid excessive weight being placed on the higher latitudes (where the convergence of the grid results in disproportionately larger numbers of data values), these latitudes were subsampled by taking only one value at 90°N, four at 85°N, eight at 80°N, and 18 at 75°N. Finally, all values south of 15°N, all values south of 30°N from 10°W to 110°E, and all values south of 45°N from 40°E to 110°E were discarded.

genities during the early period (Jones, 1987; Rogers, 1990), pre-1922 data were not used. For the UKMO data set, all values south of 20°N or poleward of 75°N were discarded; and, prior to 1950, all data from 110°E round (in an eastward direction) to 60°W at the latitudes of 70°N and 75°N were also discarded (for reasons given by Jones, 1987). Despite this removal of suspect data, our analysis (described later) strongly suggests the existence of remaining errors in the UKMO data set, so we used the GMSLP data set, for the period 1922–98, to characterize the major patterns of large-scale SLP. These latter data are available on a 5° latitude by 5° longitude grid, and mean SLP for each April–September season was computed for each grid point from the individual monthly means. To avoid excessive weight being placed on the higher latitudes (where the convergence of the grid results in disproportionately larger numbers of data values), these latitudes were subsampled by taking only one value at 90°N, four at 85°N, eight at 80°N, and 18 at 75°N. Finally, all values south of 15°N, all values south of 30°N from 10°W to 110°E, and all values south of 45°N from 40°E to 110°E were discarded.

## Spatio-temporal patterns of tree-ring density and climatic data

### Temperature calibration of the tree-ring density at the grid-box scale

The gridded tree-ring density data, produced and described by Osborn *et al.* (2002), were used in this study. The use of gridded

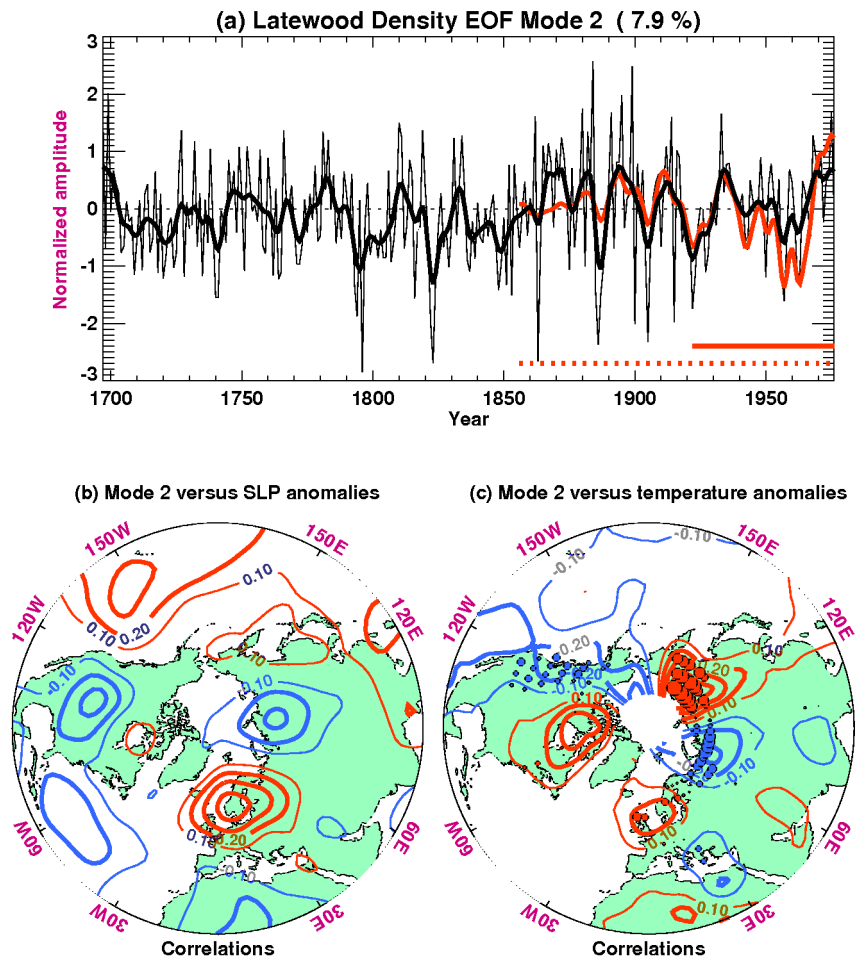


**Figure 4** As Figure 3, but for the second MXD PC.

data is designed to reduce the dominance of clusters of nearby chronologies in the Principal Component Analysis (PCA) that we use as the fundamental technique in this investigation (see later). Gridding the data also maximizes the quantity of data that can be used, by combining different length chronologies into single grid-box time series rather than having to discard the shorter chronologies that would otherwise reduce the period of complete data generally required in such analyses. The gridding procedure will be described in full by Osborn *et al.* (2002). MXD chronologies that fall within each  $5^\circ$  longitude by  $5^\circ$  latitude grid box are averaged together, with a weighting that is dependent upon the number of tree cores that exist in each chronology. In boxes where the number of chronologies with data varies through time, an adjustment is made to the average time series (Osborn *et al.*, 1997) to remove spurious changes in variance. Finally, for those grid-box time series that are a little shorter than others nearby, multiple regression models are developed to extend the shorter series by using a linear combination of nearby series, with the strict proviso that a regression model is applied to achieve this, only if it explains more than 50% of the variance of the shorter series over an independent verification period.

Here, we select a subset of the gridded MXD data set to ensure no missing values. The choice of which grid boxes to retain is a balance between the requirements for both good spatial and good temporal coverage (i.e., if a longer period is chosen, fewer grid boxes will contain calibrated tree-ring data covering the entire period). The period selected for analysis is 1697–1976, for which 92 (out of a maximum of 115) chronology grid boxes have full

MXD data (Figure 1a; which also shows the 303 chronologies that contribute to these 92 boxes). Extending the period towards the present by 1, 2 or 3 years (to 1977, 1978 or 1979) results in the loss of three, four or eight grid boxes; by 1984, only 55 boxes would be left. Similar rapid fall-off in the number of boxes also occurs if they are required to have data prior to 1697.

The gridded MXD maps have also been calibrated directly in terms of April–September temperature by use of the appropriate gridded instrumental data (Osborn *et al.*, 2002). Each MXD grid-box time series is scaled so that its variance matches that of the instrumental record from the same grid box (or from the average of the surrounding boxes, if the co-located box has insufficient data), and adjusted so that its mean also matches that of the instrumental series. As the instrumental series are expressed as  $^\circ\text{C}$  anomalies from the 1961–90 reference mean, the calibrated MXD series have the same units. This calibration does not affect the results here, since the PCA is performed on the correlation matrix of the gridded data set (i.e., the local calibration is effectively removed by normalizing each grid box time series prior to analysis). What does affect the results slightly, however, is that during the calibration procedure Osborn *et al.* (2002) make an artificial *ad hoc* adjustment to remove the dominant spatio-temporal structure of the recent relative 'decline' in high-latitude MXD. This is a gradual divergence in MXD relative to the growing-season temperatures, increasingly apparent over recent decades, that is caused by some unidentified non-temperature forcing of tree growth in certain high-latitude regions (Briffa *et al.*, 1998b). The adjustment has no significant influence on the

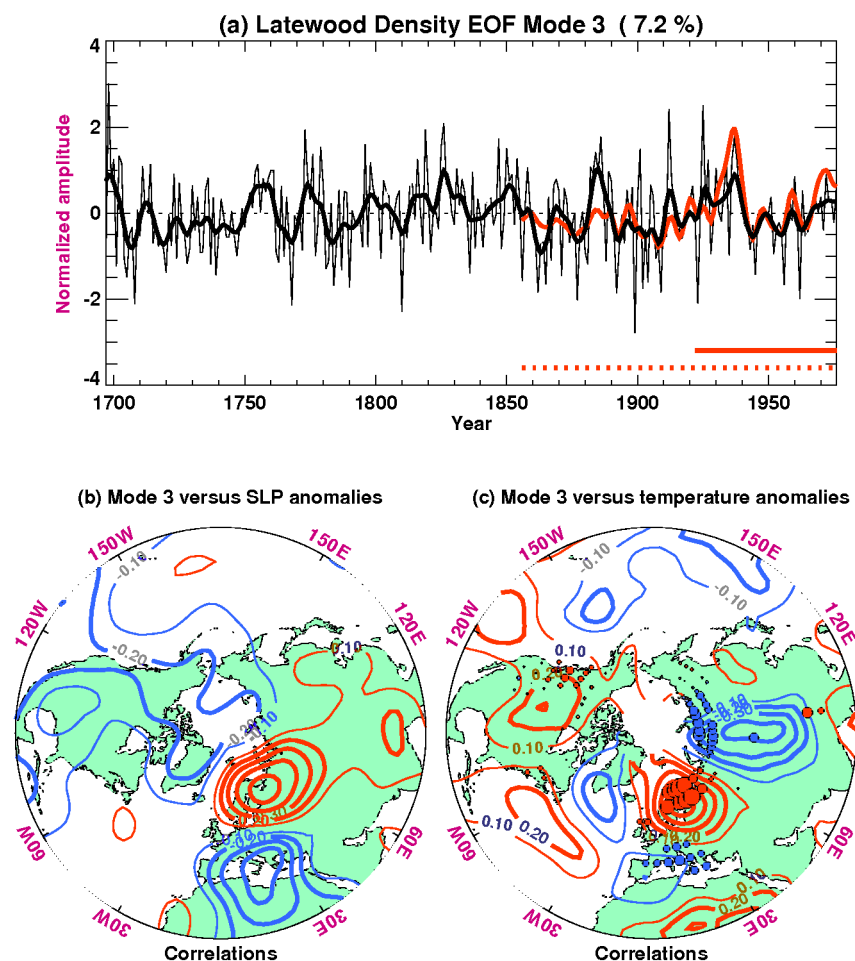


Figure 5 As Figure 3, but for the third MXD PC.

spatial patterns obtained by PCA here, and the only principal component (PC) time series that is affected is the leading PC and then only during the post-1950 period.

#### A series of summer half-year temperature maps

The main analyses presented here, exploring the relationships between large-scale density variability and associated patterns of temperature and precipitation variability, make use of the gridded MXD data as described. For climate reconstruction purposes it is also possible to produce reconstructions for regions where there are no tree-ring chronologies, provided that a relationship exists between climate in these grid boxes and other regions that do contain tree-ring information, allowing the tree-ring PCs to be used as predictors in multiple linear regression models (e.g., Fritts, 1976; Briffa *et al.*, 1986; Cook *et al.*, 1994). Figure 2 shows part of the longer series of maps where this approach was used by Osborn *et al.* (2002) to provide a greater spatial coverage of temperature estimates than that represented by the MXD network.

Here we show 288 yearly maps covering the period 1600–1887. The number of tree-ring sites is lower in the earlier period (much more so in the pre-1600 period not shown here) so that the spatial coverage increases through time. Individual grid-box estimates have greater uncertainty than larger regional averages (such as those shown in Figure 11 of Part 1) but the values in each box are independently generated so that spatially coherent clusters of similar colours (perhaps over 1000 km or more) are likely to provide a reliable indication of the location and relative magnitude of significant temperature anomalies.

The maps demonstrate the prevalence of complex temperature patterns over a range of spatial and temporal scales. While there

is no year when all regions are ubiquitously warm or cool, the base period used here (1961–90) is relatively warm overall compared to the long-term mean, so the maps will tend to exhibit more negative values than would be the case if they had been expressed relative to a long-term average. Even allowing for this, it is possible to recognize that years in which widespread cool conditions clearly predominate occur with a greater frequency than warm years. The most distinct cool years are 1601, 1642, 1695, 1742, 1816 and 1817. It is well documented that these coolings are most likely the result of volcanic eruptions (Briffa *et al.*, 1998a, and references therein). Markedly warm years are fewer, but 1846 and 1878 are the most prominent. Much more common are years when distinct large regional anomalies can be identified, such as strong warmth (1629, 1640, 1652, 1703, 1831, 1858) or cold (1614, 1632, 1647, 1705, 1790) centred on Fennoscandia, almost always associated with an anomaly of opposite sign to the east, over western Siberia, implying related anomalous advection of warm or cold air around persistent anticyclones.

#### Methods for linking MXD and associated climate variability

Principal component analysis was used to identify the leading modes of variability exhibited by the maximum latewood density data. The analysis was based on the correlation matrix of the data set, computed over the period 1697–1976, during which time the 92 grid boxes shown in Figure 1a had complete data. Rotation was not applied to the resultant PC loading patterns, because varimax rotation (Kaiser, 1958) resulted in loading patterns with single centres of action very similar to the regional-mean time series already reconstructed in Part 1. The leading eight PCs capture a

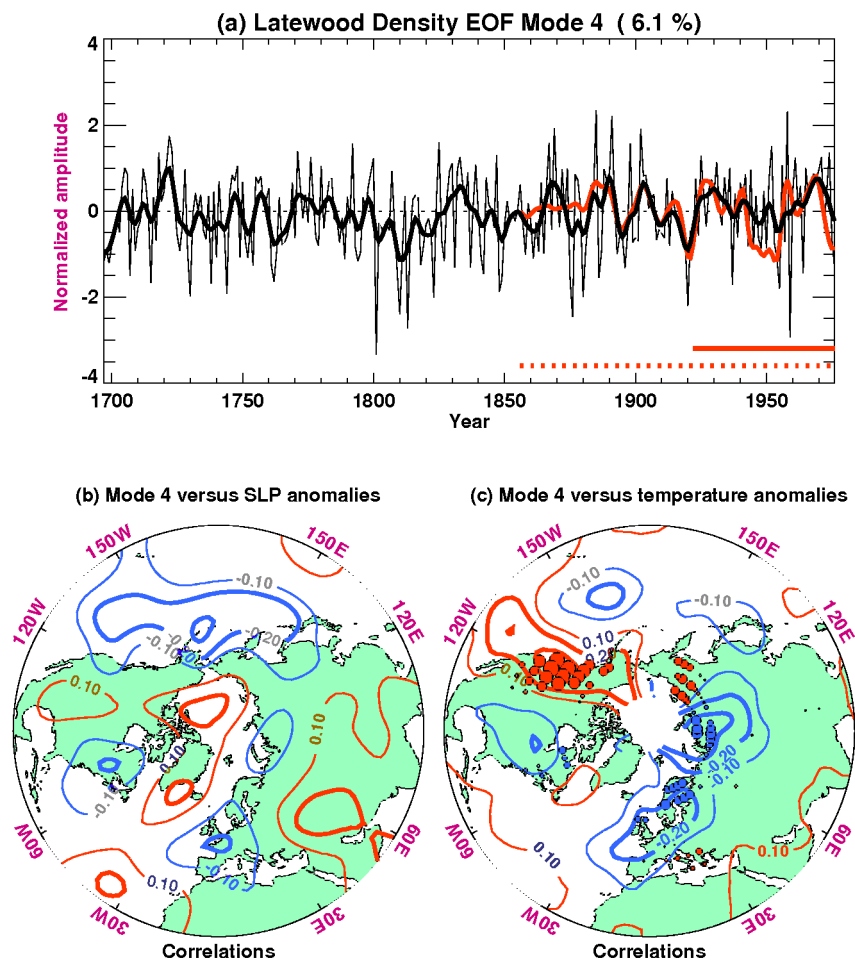


**Figure 6** As Figure 3, but for the fourth MXD PC.

little over 50% of the variance in the MXD data set (Table 1), and are shown in Figures 3–10 (time series in (a), loading patterns shown by dots in (c)).

The relationship between each mode and surface climate variability was identified by correlating each PC time series, first with the grid-box SLP and then the temperature series, and mapping the correlation coefficients (contours in (b) and (c), respectively, of Figures 3–10). The temperature time series were also regressed upon each normalized PC time series, and the patterns of regression slope coefficients (not shown) were scaled in a similar way to PC loading patterns (i.e., to represent a multivariate vector with unit length). The temperature data set was then projected onto these patterns (by computing the dot product between each yearly temperature anomaly field and the scaled pattern of regression coefficients), to obtain time-series that measure the evolving expression of each temperature pattern in the full temperature data set (in the same way that MXD PC time series measure the evolving magnitude of MXD loading pattern in the full MXD data set). These temperature time series are shown, after decadal smoothing, by the red curves in Figures 3a–10a. Note that the incomplete spatial coverage of the temperature data set, especially prior to the twentieth century, could introduce bias to the time series.

One measure of the strength of the association between the MXD loading patterns and the corresponding April–September temperature patterns (i.e., the dots and contours respectively in Figures 3c–10c) is the correlation between the MXD PC time series and the time series associated with the corresponding temperature patterns (computed as described above). These correlations (Table 1) remain high for the leading eight PCs,

indicating that the association between MXD and April–September temperature is very strong. Indeed, these correlations are stronger than many of the local correlations with temperature evident in the MXD data set (see Figure 5 of Part 1); in the same way that computing regional averages strengthens the signal-to-noise ratio and raises the correlation with climate, the leading modes of variability also combine data in the spatial sense and thereby similarly enhance the signal-to-noise ratio.

How meaningful, however, are the correlations given in Table 1? They compare the time series associated with the MXD and temperature patterns shown in Figures 3c–10c, but, because the temperature patterns were themselves defined from the MXD PC time series, the correlations might be expected to be high regardless of any climate signal in the MXD data. To test this, the MXD time series were replaced with red or white noise time series (i.e., completely unrelated to climate) and the same analysis procedure used. This results in arbitrary temperature patterns whose associated time series turn out to be *uncorrelated* with the ‘noise’ time series used, showing that the high correlations in Table 1 are entirely due to the strong temperature signal in the MXD data.

If a similar procedure is applied to estimate the time series associated with the sea-level pressure patterns (Figures 3b–10b) obtained by regression against the MXD PC time series, then correlations obtained between these and the MXD PC time series are in the range 0.48 to 0.71. These are almost as high as those obtained for the temperature patterns (Table 1), indicating an apparently strong link between the dominant modes of MXD variability and anomalous summer atmospheric circulation. For SLP, however, even random (red or white noise) time series result

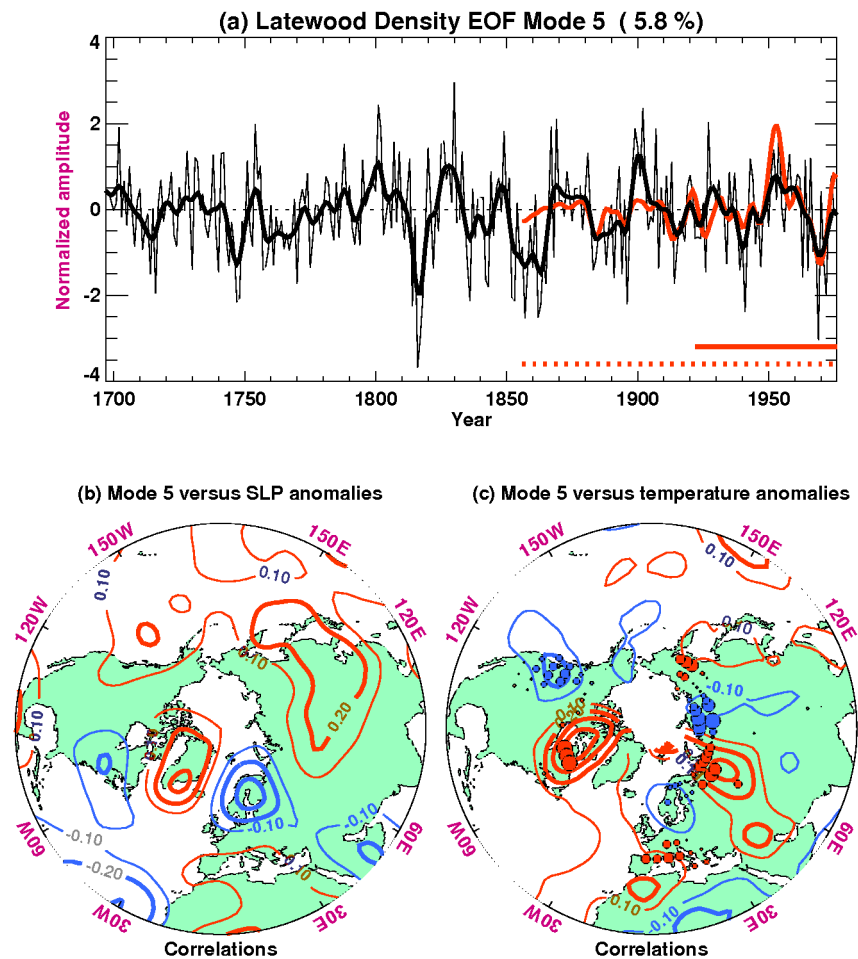


Figure 7 As Figure 3, but for the fifth MXD PC.

in correlations in the range 0.39 to 0.66, demonstrating that the link between MXD and SLP is, in fact, only slightly stronger than that expected by chance. The random series result in higher correlations for SLP than for temperature because the possibility of overfitting is higher for SLP, given the reduced number of spatio-temporal degrees of freedom: a consequence of the shorter time series (1922–76 only); fewer grid boxes; and greater spatial coherence. Repeating the analysis, but using the PCs of land air temperature (rather than the PCs of MXD), results in correlations that are higher than those obtained by chance for only the leading five modes. These results highlight the relative weakness of the relationship between air temperature over land and atmospheric circulation during the warm half of the year, and the need to carefully test any reconstructions of circulation variability to guard against the possibility of overfitting given the short observational data set that is available.

### Modes of tree-ring density variability

The leading mode of variability evident in the MXD data (Figure 3) explains 12% of the data set variance during the 1697–1976 period, and has positive loadings everywhere. The amplitude series represents hemispheric warming or cooling, and correlates very highly with the hemispheric reconstruction shown in Part 1, the main difference being that the PC time series does not show a strong decrease since 1950. This is entirely due to the artificial adjustment that was made to the post-1950 gridded MXD data used here (see earlier section on ‘Temperature calibration...’). Figure 3 shows the summer Northern Hemisphere warming from 1920 to 1940, plus the cool summers following explosive volcanic eruptions (see also Briffa *et al.*, 1998a). Both spatially and

temporally, there is excellent correspondence with the observed temperature variations, with the contours in Figure 3c following some of the variation in the magnitude of the loading pattern (e.g., the Scandinavian and northwest Russian maximum). There are positive correlations with temperature across most of the hemisphere, the main exception being over the eastern half of the North Pacific Ocean. The association with April–September circulation (Figure 3b) is weak, probably because this mode is primarily a response to external forcings rather than anomalous circulation.

The strongest centres of action in the second MXD mode (Figure 4) indicate an east–west temperature dipole in northern Russia that corresponds closely with the observed temperature pattern (which is especially strong in eastern Siberia, despite the poorer temperature correlations exhibited by individual chronologies in this region – see Part 1). The other, less important, centres of action in Europe and North America are also well correlated with observed temperatures. The time evolution of this mode is not significantly correlated with temperature over the oceans, but there is a strong relationship with SLP (Figure 4b); the anomalous circulation implied by the SLP correlations being entirely consistent with the temperature and MXD anomalies (i.e., southerlies over warm areas, northerlies over cold areas). This anomaly pattern is clearly identifiable in those yearly maps (Figure 2) when the PC time series (Figure 4a) has large values (e.g., a reversed pattern is clear in the 1796 reconstruction, a year with a strong negative PC value).

The third principal component of MXD (Figure 5) is associated with variations in the strength of westerlies that influence the temperature in northern Europe. There is, once again, good correspondence between the MXD and temperature patterns, the only minor

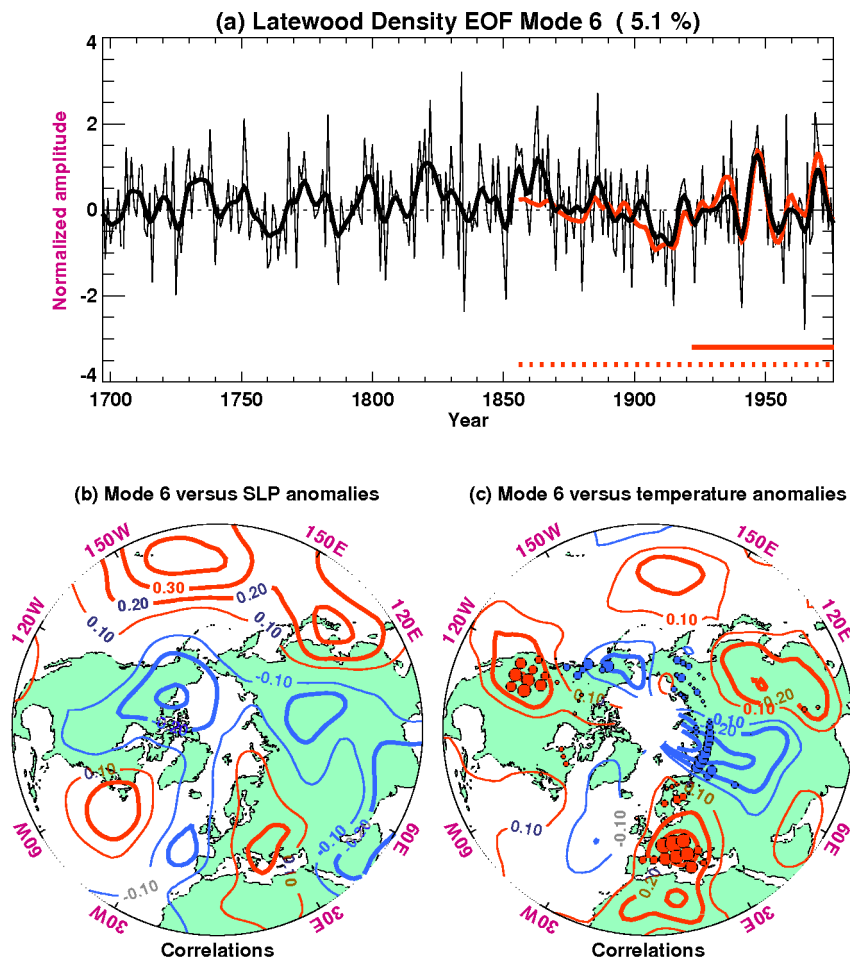


Figure 8 As Figure 3, but for the sixth MXD PC.

discrepancies being in southern Europe and the Tibetan Plateau. There is good agreement between the temporal evolution of the MXD and temperature patterns (Table 1; Figure 5a). This pattern is particularly prominent in the 1698 reconstruction (Figure 2), a year with a high amplitude for this PC (Figure 5a).

The fourth mode (Figure 6) is a dipole between MXD anomalies of one sign over western North America and eastern Siberia, and anomalies of the opposite sign over northern Europe and central northern Siberia. With the exception of eastern Siberia, temperature and MXD patterns are in close agreement. The temporal variability in the strength of this pattern is correlated with variations in the strength of the Aleutian Low, perhaps explaining the western North American MXD and temperature signals. The largest negative value in the time series occurs in 1801, and a strong, reversed pattern is evident in the reconstructed map for that year (Figure 2). There is little low-frequency variability evident in the PC time series of this mode (Figure 6a).

The fifth principal component of MXD (Figure 7) shows the weakest link with temperature (Table 1), as measured by the correlation between the PC time series and the evolution of the associated temperature pattern. The sign of the loading pattern is well matched by the sign of the correlations with temperature, but the magnitudes are a poorer match (e.g., in the eastern Mediterranean and in central and eastern Siberia). The largest anomalies in the PC time series occur during the 1810s, following the eruption of Tambora in 1815, though similar negative anomalies do not appear after other volcanic eruptions (e.g., the late 1690s, 1884). This mode may, therefore, partly represent the particular spatial characteristics of the cooling that followed the large Tambora eruption.

Three further modes are also shown in Figures 8–10, principally to illustrate the continuing agreement between the higher order MXD loading patterns and the pattern of temperature correlations, even down to the minor modes, each of which explains 5% or less of the overall data set variance. With the exception of the region of eastern Siberia, the correspondence remains excellent. The strength of the SLP pattern associated with each mode shows considerable variation from mode to mode, as does the physical interpretation. For mode 8, for example, the variation in the meridional circulation over Europe (Figure 10b) can be simply linked with the spatial structure of the European MXD and temperature anomalies (Figure 10c), yet the cause of the anomalies in eastern Canada is somewhat harder to establish.

## Reconstructing summer circulation patterns

### Identifying characteristic modes of summer atmospheric circulation

There are different approaches that can be adopted for estimating the nature of past atmospheric circulation variability using high-resolution proxy climate data. Separate statistical models could be developed to predict the time series of SLP at individual grid points, with the estimated time series then being combined to provide the SLP patterns, year by year, over an extended region (equivalent to the 'point-by-point' approach used to reconstruct drought patterns over the USA by Cook *et al.*, 1999). This approach has not been used to date for reconstructing MSLP. Direct linear regression, involving multiple tree-ring predictors,

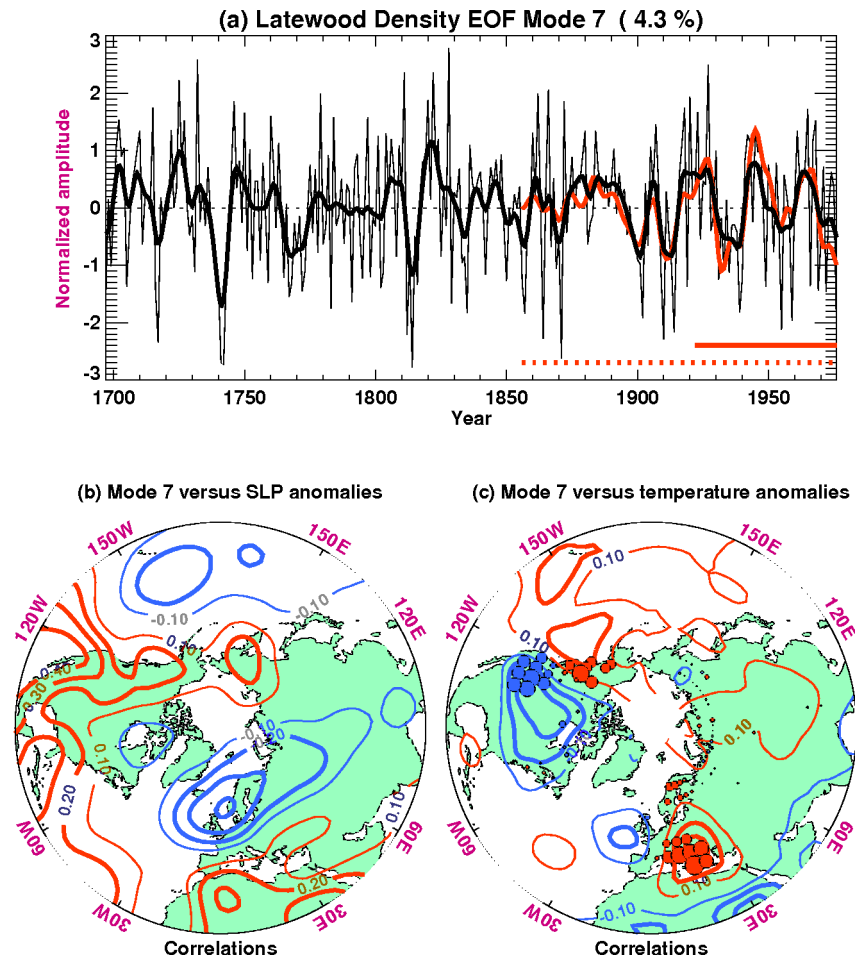


**Figure 9** As Figure 3, but for the seventh MXD PC.

has often been used to reconstruct regional pressure index series (e.g., pressure gradients between key locations). Examples include the indices of the North Atlantic Oscillation (Cook *et al.*, 1998; 2002), the Southern Oscillation Index (Stahle *et al.*, 1998); the Southern Hemisphere Transpolar Index (Villalba *et al.*, 1997) and zonal and meridional pressure indices over New Zealand (Salinger *et al.*, 1994). Another approach that has been proposed is the direct reconstruction of the frequency of specific synoptic weather types (Hirschboeck *et al.*, 1996). However, for reconstructing large-scale pressure patterns, following the pioneering work of Fritts *et al.* (1971; see also Fritts, 1991) reconstructing pressure variability over the eastern Pacific and western North America, it has been more common in dendroclimatic studies to develop principal-component-based regression models to predict the year-by-year indices of each of an objectively defined set of characteristic large-scale modes of SLP variability (Briffa *et al.*, 1986; Cook *et al.*, 1994).

We first explore the characteristic (i.e., persistent and/or recurrent) modes of April–September mean atmospheric circulation variability for the Northern Hemisphere. Specification of the season is important because the dominant patterns of circulation variability vary between the seasons. Barnston and Livezey (1987; hereafter BL87) show that only one out of the 13 SLP modes that they identify is evident in all individual months of the year, and, because April–September is not a standard season, the relevance of earlier descriptions of major hemispheric SLP modes is limited. For example, Wallace and Gutzler (1981) and similar studies only consider the winter, while BL87 analyse 700 hPa height fields for all months individually but identify only five modes characteristic of the warm or transition seasons (compared

with nine cold-season modes), and, of these five, only the North Atlantic Oscillation was clearly identified in all months from April to September. Rogers (1990; hereafter R90) provides more encouragement, finding seven modes of monthly SLP variability that can be identified in three or more of the months from April to September. To simply average together the April–September time-series associated with each of the monthly modes identified by R90 is inappropriate, because two of the modes are undefined for some months and for the other modes the patterns exhibit some rather large month-to-month differences (e.g., compare Figures 4b and 4c of R90).

Here we follow the approach of R90 to explore mean summer half-year atmospheric variability – i.e., varimax-rotated PCA (Kaiser, 1958) is applied to the mean April–September SLP fields of the UKMO and GMSLP data sets. BL87 outline the advantages of rotating the principal components in this context. We use SLP rather than geopotential height fields, because the latter are too short to provide a sufficiently long period of overlap with the tree-ring data to allow adequate calibration and verification of the reconstructions.

If PCA is applied to the 74-year period from 1922 to 1995 of the UKMO SLP data, then over 40% of the spatial coverage is lost due to small amounts of missing data in many areas. Instead, the seven years with most missing data (1922, 1931, 1938–40, 1942 and 1946) are omitted, because more than 90% of the grid points have full data for the remaining 67 years. Using the selection criterion of a discontinuity in the ‘scree diagram’ (a plot of the logarithms of the eigenvalues), the leading nine PCs of this 67-year data set are retained and rotated, capturing 63% of the total variance in the data set. Estimates of the principal component

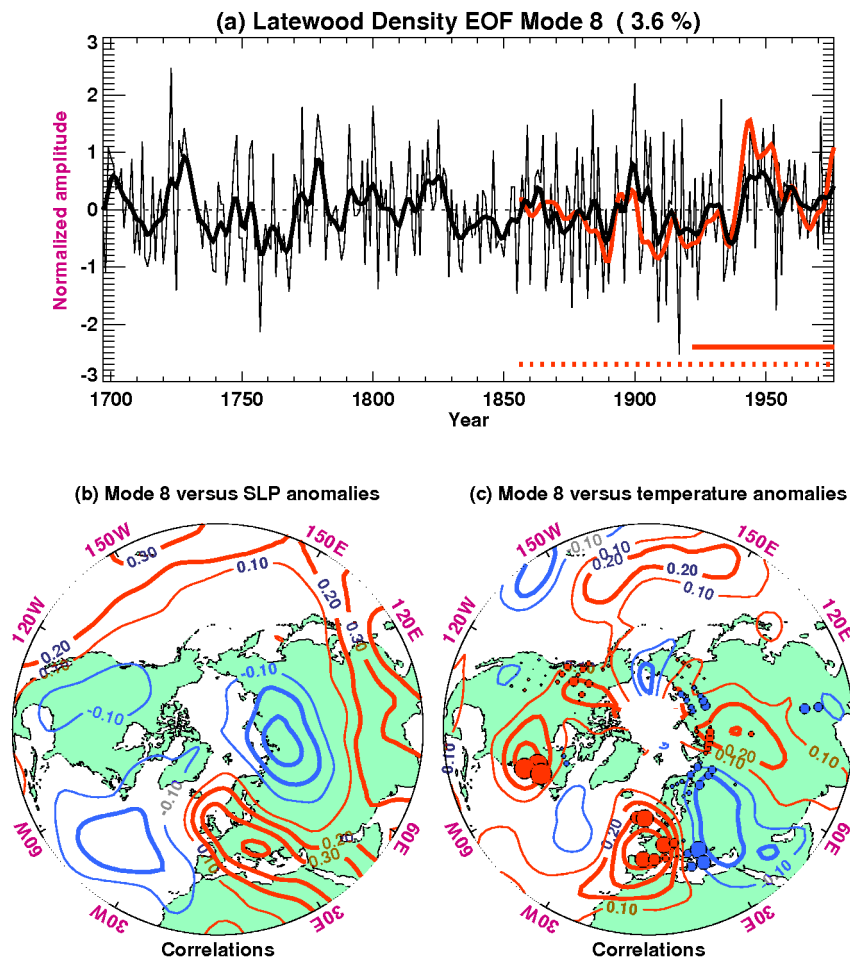


Figure 10 As Figure 3, but for the eighth MXD PC.

**Table 1** MXD variance (%) captured by the leading MXD principal components, and the correlation (over 1856–1976) between each MXD PC time series and the time series associated with the corresponding temperature pattern

PC no.	variance (%)	$r$
1	12.1	0.71
2	7.9	0.60
3	7.2	0.73
4	6.1	0.61
5	5.8	0.57
6	5.1	0.73
7	4.3	0.63
8	3.6	0.69

time series are made for the seven omitted years, by projecting the available SLP data for those years onto the corresponding subset of the principal component loading pattern (Kelly *et al.*, 1999). It should be expected that some data errors will remain, even after the removal of some data-poor or data-sparse regions, but they are likely to be small in scale or have low variance, having little effect on the PCA. However, a *large-scale* data problem is apparent, in the form of the leading rotated component (Figure 11), accounting for 13% of the variance (this mode also appears as the leading mode *before* rotation). The small-scale spatial structure in the pattern, and the tendency for the highest loadings to be over either high-elevation regions (the western and central USA; the Atlas

Mountains; and the Tibetan plateau) or the tropical oceans (with known errors (R90) in warm-season SLP during the first half of the century) indicate that this is unlikely to be a real mode of variability. The time series associated with this mode (Figure 11) has a strong downward trend throughout the period, perhaps with more rapid reductions around the early 1940s, 1970 and the early 1980s. Further work is needed to clarify the source of this PCA pattern, but here we simply choose to concentrate on the GMSLP data set instead, which has benefited from additional homogenization (Basnett and Parker, 1997).

The GMSLP data set is complete over our analysis region (being based on sources additional to those of the UKMO analyses, and with statistical infilling of missing values) and so our full analysis period (1922–98) was subjected to PCA. A discontinuity in the scree diagram suggested that the leading eight components should be retained and rotated; these eight modes (Figures 12 to 19; patterns in (a) and time series in (d)) capture 65% of the total data set variance. None of the components show a pattern or temporal evolution that is similar to the leading UKMO mode (Figure 11), lending further weight to our suggestion that the UKMO data contain spurious long-term trends, and demonstrating that these have been removed from the GMSLP data. The GMSLP modes appear to represent physically meaningful atmospheric circulation variations, and partly match previously identified modes. Comparison is made visually between Figures 12–19 and the patterns published by R90, and quantitatively by correlation between the PC time series and the time series associated with the transition/warm season modes identified by BL87 and updated by the US Climate Prediction Center (<http://www.cpc.ncep.noaa.gov/data/teledoc/telecontents.html>).

The dominant Atlantic modes are split into mode 1 (Figure 12;



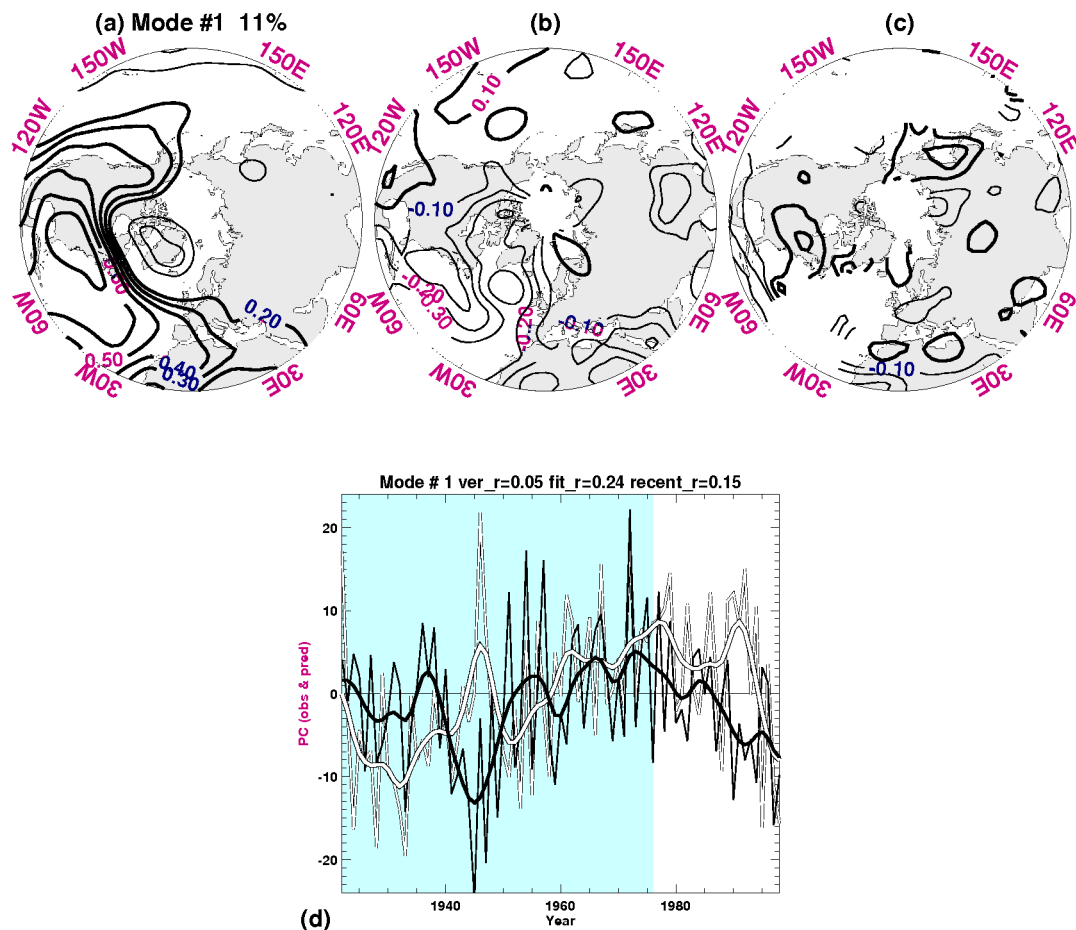


**Figure 12** Correlations between the first PC (following varimax rotation) of April–September SLP (from the GMSLP3.2 data set) and April–September (a) SLP; (b) land air temperature and SST; (c) land precipitation. Contour interval is 0.1; zero contour is omitted (as are  $-0.1$  and  $0.1$  in (a)); thick contours indicate positive correlations; thin negative. The percentage of the SLP variance captured by this PC is given in (a). (d) The PC time series (white curve outlined in black), with decadal smoothed values (thick curve), together with a reconstruction attempted using instrumental temperature PCs as predictors (black curve, with thick black curve after decadal smoothing). Grey shading indicates the period (1922–76) used for calibration and verification exercises: 60% of grey period was used for screening regression and the remaining 40% was used for independent verification (verification correlation given by ‘ver\_r’); recalibration was then performed over the full grey period (calibration correlation given by ‘fit\_r’); and a separate independent verification calculated over the recent unshaded period (‘recent\_r’). No reconstruction is shown using tree-ring density PCs as predictors, because none passed the screening regression (Table 2).

similar pattern to the Bering Sea mode of R90. Mode 7 (Figure 18) correlates moderately with the *Asian Summer* time series of the updated BL87 analysis and has a clear spatial similarity with that mode. Mode 8 (Figure 19) has similarities with the *Scandinavian* pattern of R90 and correlates well with the *East Atlantic Jet* that is identified in the updated BL87 analysis.

### Assessing the potential for reconstructing atmospheric circulation

In the introduction, and in the discussion above concerning the occurrence of characteristic modes of MXD variability, the strength of the link between surface temperature and atmospheric circulation was considered. It is weaker in summer than in winter. A question that needs to be addressed, therefore, is: ‘what is the potential for reconstructing summer circulation, given a knowledge of summer temperatures over land?’. This will give an upper bound on the expected skill of reconstructions based on the tree-ring density data set, given that they are imperfect estimates of summer temperatures. An initial indication of the strength of the link between each atmospheric circulation mode and surface temperature is given by the correlations (Figures 12b–19b) between local temperatures and each SLP PC time series. The local correlations are fairly weak overall, rarely exceeding  $\pm 0.3$  over the land (stronger correlations occur more frequently over the ocean). Thus, any usable reconstruction must rely on integrating infor-

mation spatially, because a predictor at a single location will have insufficient skill. A subjective assessment of correlation strengths and extent over land suggests that SLP modes 2, 4, 5, 7 and 8 may be the most predictable if using only land air temperatures.

Principal components regression was used to reconstruct each of the SLP modes in turn. PCA of the April–September land air-temperature data was performed for the period 1922–98 and for the region shown in Figure 1b. The leading eight PCs (not shown) were provided as potential predictors to a stepwise screening multiple regression procedure (e.g., Draper and Smith, 1981: 307). Predictors enter (and remain in) the regression equation only if their partial correlation with the predictand exceeds the 0.05 significance level (the entry/exit threshold). The 1922–76 period is split 60:40 into 33 years for calibration and 22 years for verification (further details are given in Table 2). Thus, even though values of both the predictors (temperature PC time series) and the predictands (SLP PC time series) are also available for 1977–98, these data were not (initially) used in order to reproduce the situation that applies to the MXD data (for MXD the PC time series stop in 1976, due to a rapid reduction in spatial coverage after that). The stepwise regression model is built solely on the calibration period, and independently tested over the verification period (correlations are given in Table 2). For the successful cases, the regression model was then recalibrated over the full (1922–76) period (calibration correlations are also given in

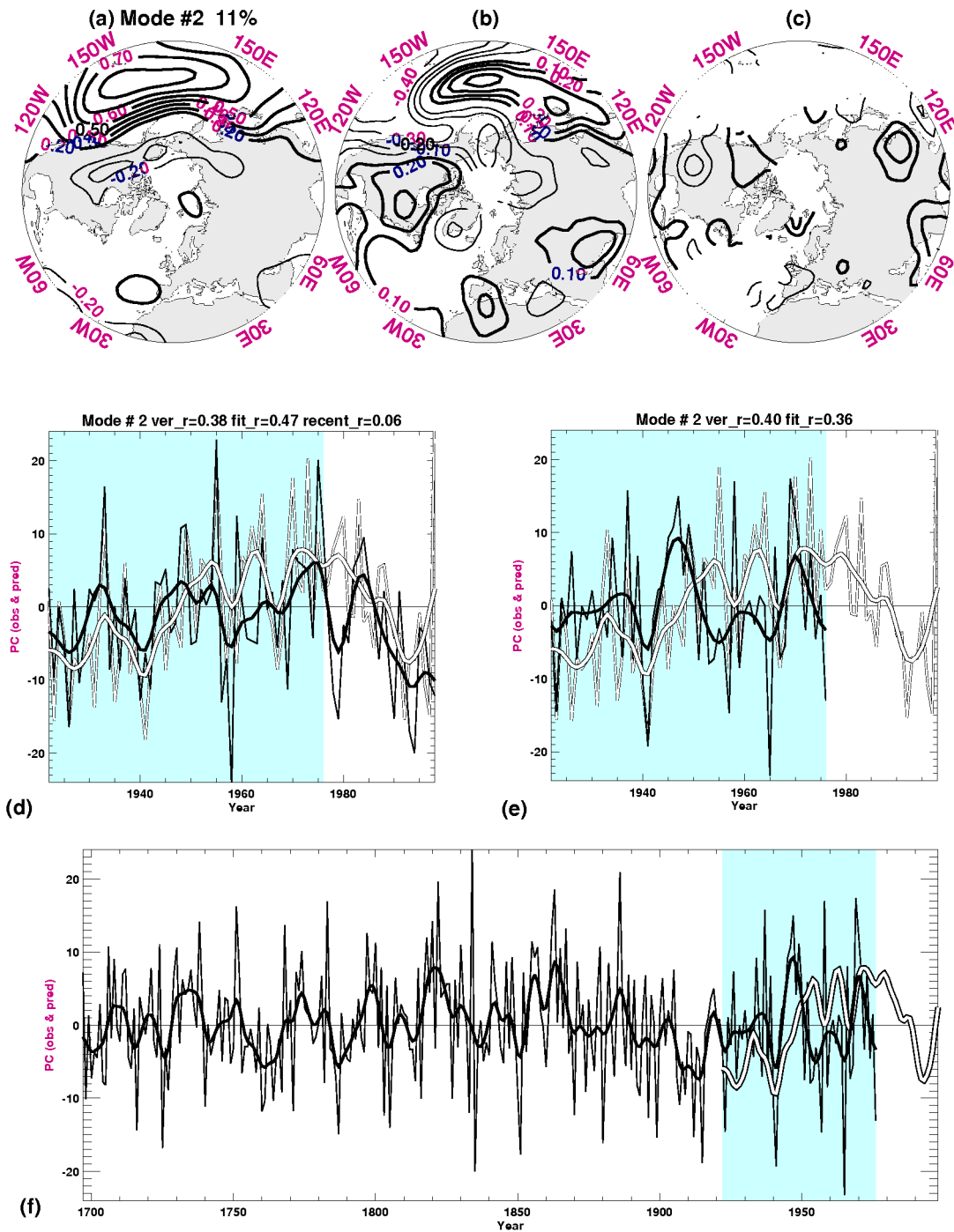


**Figure 13** As Figure 12, but for the second rotated PC of the SLP data; also shown is a reconstruction attempted using tree-ring density PCs as predictors. (e) As for (d), except that tree-ring density PCs stop in 1976, so there is no verification over the recent unshaded period. (f) as for (e), except showing the full reconstruction back to 1697, and only the smoothed observed PC time series is shown (1922–98).

Table 2), and a supplementary verification was possible for the 1977–98 period that had previously been withheld.

Of the eight SLP modes attempted, one failed because none of the eight candidate predictors passed the entry threshold, and two failed because their verification correlations were not significant (in fact, the latter two were recalibrated over the longer period despite the poor verification, but they still failed in the supplementary verification). The predicted time series are compared with the actual series in Figures 12d–19d (except for mode 3, Figure 14, for which no prediction could be made). Of the five that were successfully reconstructed (modes 2, 4, 5, 7 and 8, matching our subjective *a priori* assessment of those modes with most potential for reconstruction – see earlier), the verification correlations vary from 0.38 to 0.72, and the overall recalibration correlations from

0.47 to 0.77, indicating an apparently useful level of skill. The supplementary verification is useful, however, because it demonstrates the ease with which overfitting can occur when using short data samples, even with careful and independent verification. Of the five ‘successful’ predictive models, only three pass the supplementary verification (by achieving significant correlations). The three SLP modes for which we consider the temperature-based predictive models to be reliable, based on the statistics given in Table 2, are modes 5 (with no direct match to previously published modes), 7 (the Asian Summer mode of BL87) and 8 (the R90 Scandinavian or BL87 East Atlantic Jet mode).

The level of skill and number of successfully predicted modes, while useful, is not very high, given that real temperatures were used as predictors. We believe that this is due to a combination

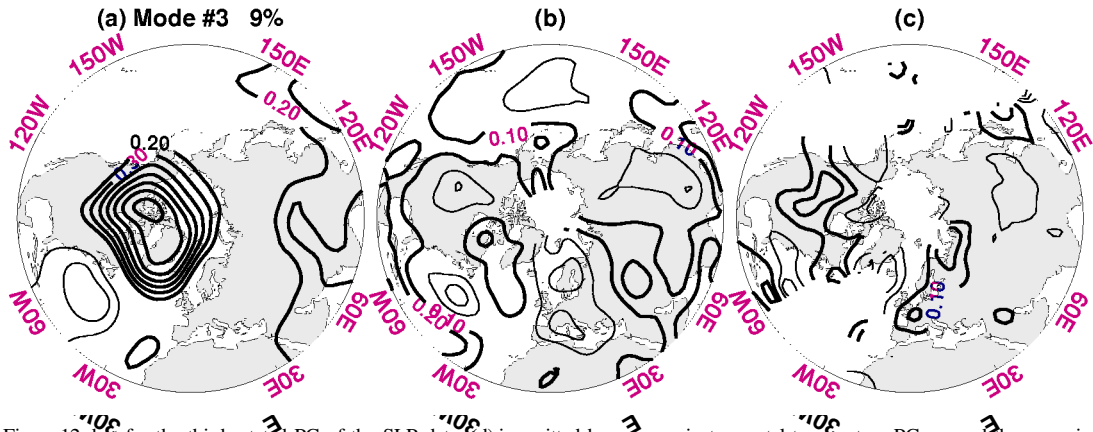


Figure 14 As Figure 12, but for the third rotated PC of the SLP data; (d) is omitted because no instrumental temperature PCs passed the screening regression.

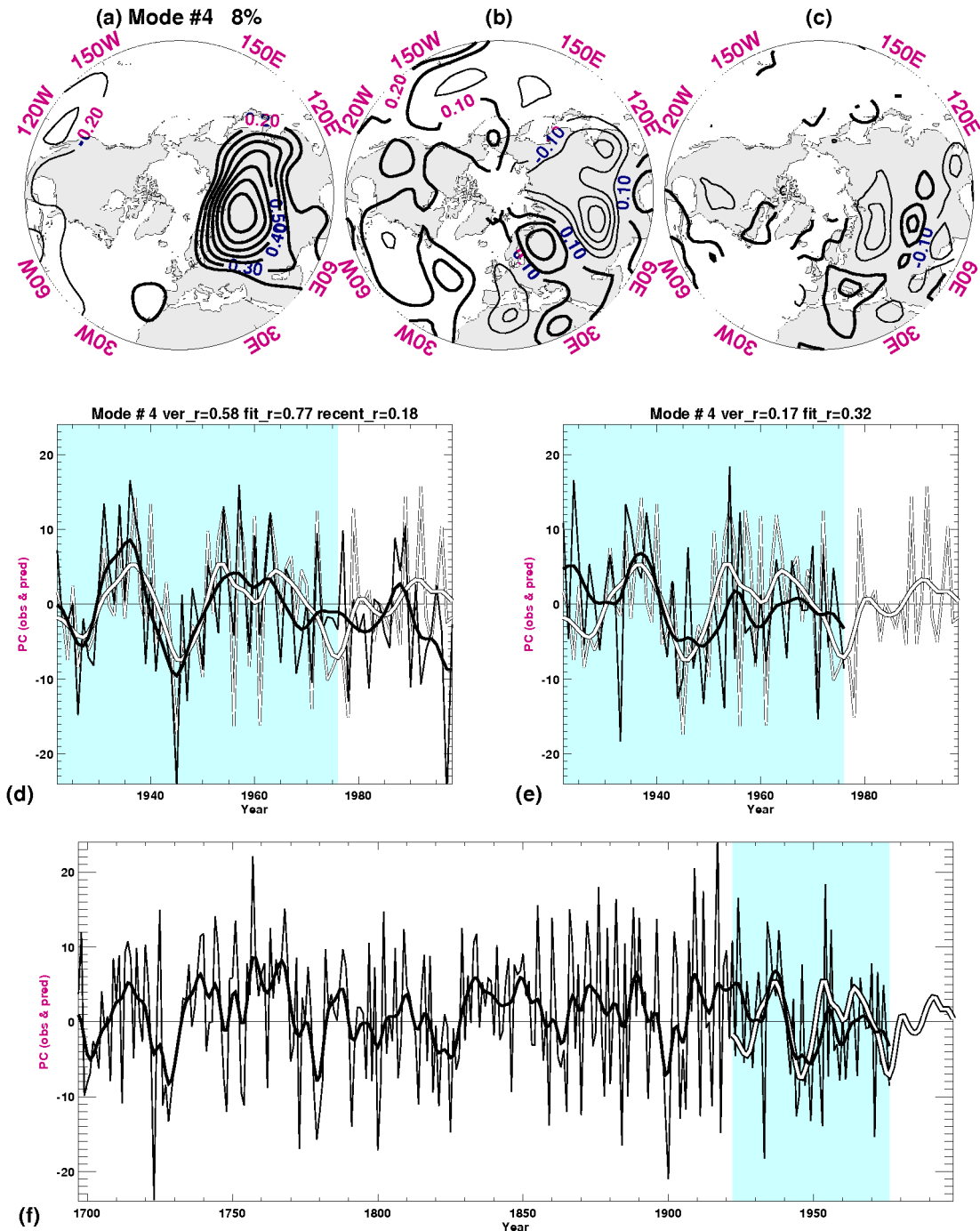
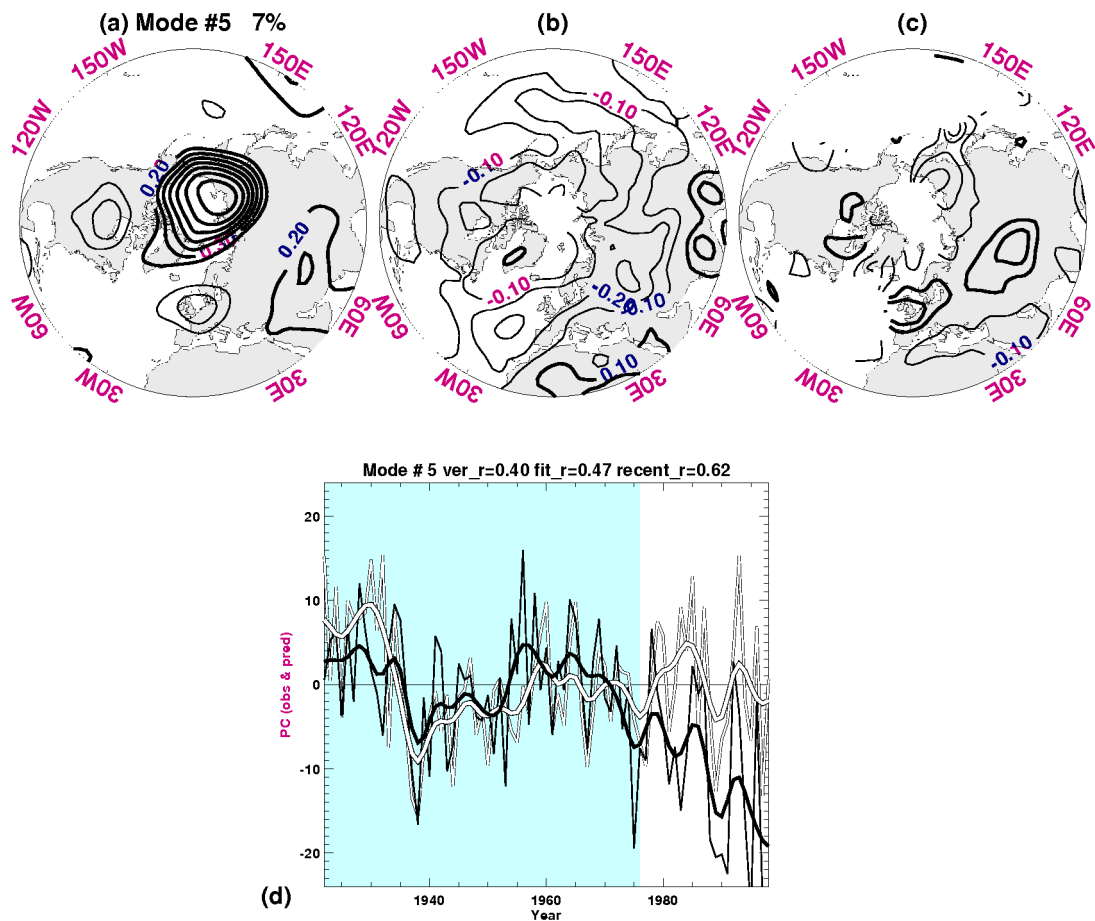


Figure 15 As Figure 13, but for the fourth rotated PC of the SLP data.



**Figure 16** As Figure 12, but for the fifth rotated PC of the SLP data.

of a relatively weak temperature–circulation relationship in summer, and short data samples for fitting and testing the predictive models. We note also that the results presented in Table 2 show, for some modes at least, worrying sensitivity to the choice of calibration and verification periods, reducing further our overall confidence in the reconstructions. The correlations obtained for the temperature-based models represent the benchmark for evaluating the skill of the reconstructions based on the MXD data set, because it is unlikely that the MXD data would do better than real temperatures. We note, though, that additional predictor variables may improve the reconstruction skill (e.g., Figures 12c–19c show the correlations with land precipitation for each mode, using data from Hulme, 1994). Certainly Figures 12–19 suggest that summer sea-surface temperatures are potentially important predictors for modes 1, 2 and 6, while European summer precipitation is closely related to mode 8.

### Preliminary MXD reconstructions of atmospheric circulation

The same procedure (principal components regression using a stepwise screening regression) was used to attempt reconstructions of the eight SLP modes using the MXD data as predictors. The potential predictors that were offered to the screening regression were the leading eight PC time series of the MXD data set computed over the 1697–1976 period (i.e., those shown in Figures 3a–10a). The 55-year overlap period between predictors and predictands (1922–76) is again split 60:40 into 33 years for calibration and 22 years for independent verification (further details are given in Table 2). Calibration and verification correlation coefficients are given in Table 2.

The MXD predictors can successfully reconstruct only four of the SLP modes of variability (Table 2), with the remaining four

having no predictors that pass the entry threshold of the screening regression. The time series of the four reconstructed SLP modes are compared in detail with the actual series in Figures 13e, 15e, 18e and 19e, and are shown in full in Figures 13f, 15f, 18f and 19f. All of these four were also predictable from the instrumental summer land temperatures, though two (modes 2 and 4) subsequently failed the supplementary verification over the recent period. While the calibration correlations are lower for the MXD predictors than for the temperature predictors (because more predictors passed the entry threshold in the latter case), their verification correlations are comparable (Table 2). For the four reconstructed modes, therefore, the MXD predictors are probably performing almost as well as could be expected, and the low reliability of the reconstructions is mainly due to the weak link between summer land temperature and atmospheric circulation, rather than the use of a proxy for land temperature (i.e., the MXD data).

Perhaps the main discrepancy is that SLP mode 5 (Figure 16a) performed well with the temperature predictors, but failed with the MXD predictors; this is somewhat surprising given that the temperature pattern associated with it (Figure 16b) ought to be well captured by the distribution of MXD data (Figure 1a). It should be noted, however, that the verification correlations flatter the true performance of the temperature predictors for this mode: inspection of the time series (Figure 16d) demonstrates the disagreement at low frequencies over the recent period. This is because the first temperature PC, which is the main predictor of this SLP mode (Table 2), is probably driven by the anomalous circulation at the high frequencies, but appears to have a longer-term trend (especially since the 1970s) that is likely to be driven by external forcing factors (this temperature PC, not shown, is similar to the first MXD PC shown in Figure 3, in that it has a

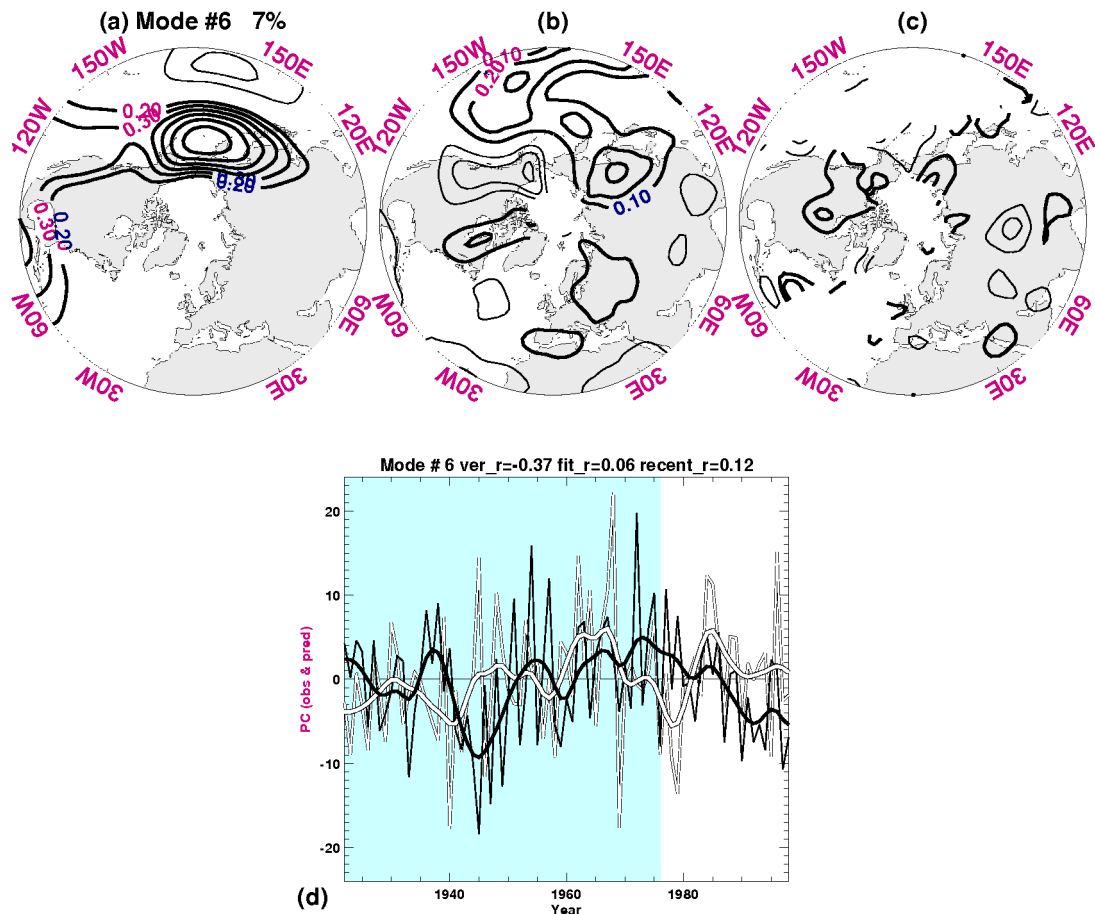


**Figure 17** As Figure 12, but for the sixth rotated PC of the SLP data.

pattern of uniform sign and a time series that matches the hemispheric-mean warm-season temperature).

The MXD-based regression models also show sensitivity to the details of the regression procedure (e.g., precise specification of calibration and verification periods), reducing our confidence in the reconstructions presented in Figures 13f, 15f, 18f and 19f. One particular concern is that the eighth MXD PC has been selected as the sole predictor for both SLP modes 4 and 7 (Table 2). The result is that the reconstructions (Figures 15f and 18f) are perfectly correlated (in fact, they are perfectly anticorrelated, but, since the sign of the SLP mode pattern and time series pair is arbitrary, so, therefore, is the sign of the regression coefficient applied to the predictor PC). This is surprising, and very probably erroneous, given that the SLP modes are supposed to represent distinct spatio-temporal patterns of atmospheric variability (they are orthogonal, by definition, in the space domain, though not strictly orthogonal in the time domain due to the use of varimax rotation). Inspection of the temperature associations of the two SLP modes (Figures 15b and 18b) in comparison with those of the MXD PC (Figure 10c) indicates partial agreement over Eurasia in both cases, while comparison of the time series (Figure 15e and 18e) shows decadal-scale agreement for SLP mode 4 and multidecadal agreement for SLP mode 7, but poorer high-frequency agreement for both. The selection of the same sole predictor for both SLP modes is probably an artifact of the short sample available for the screening regression; a longer overlap period would probably result in regression models that combine information from this MXD PC with other predictors (different in each case) to yield only partially correlated reconstructions.

## Discussion and conclusions

The spatio-temporal modes of variability evident in the maximum latewood density of a network of tree-ring chronologies, spanning many of the mid- and high-latitude regions of the Northern Hemisphere, have been presented. The MXD data have been used in a gridded form, but the information within each grid box is independent of all other grid boxes. The occurrence of spatially coherent patterns of variability is evidence, therefore, of a spatially coherent common signal affecting the tree-ring densities. This common signal has been shown (Part 1) to be the temperature during the summer half-year, and this has been confirmed here by regression of the time series associated with each MXD mode against summer-temperature data. The correspondence between MXD and temperature patterns is very high, even down to the less important modes of variability, and is stronger than many of the local MXD versus temperature correlations. The modes of MXD variability, identified by principal component analysis, thus achieve an improved climate signal (i.e., a higher signal-to-noise ratio) by spatial integration – but without having to use predefined regional averages (e.g., as used in Part 1).

Some of the MXD modes are likely to be a response to climate-forcing agents, especially the leading mode which represents coherent warming or cooling across the tree-ring network. Other MXD modes are correlated with sea-level pressure variations, and some of the MXD (and implied temperature) variations can be qualitatively attributed to advection of heat by anomalous atmospheric circulation patterns. The potential exists, therefore, to reconstruct past variations in summer half-year atmospheric

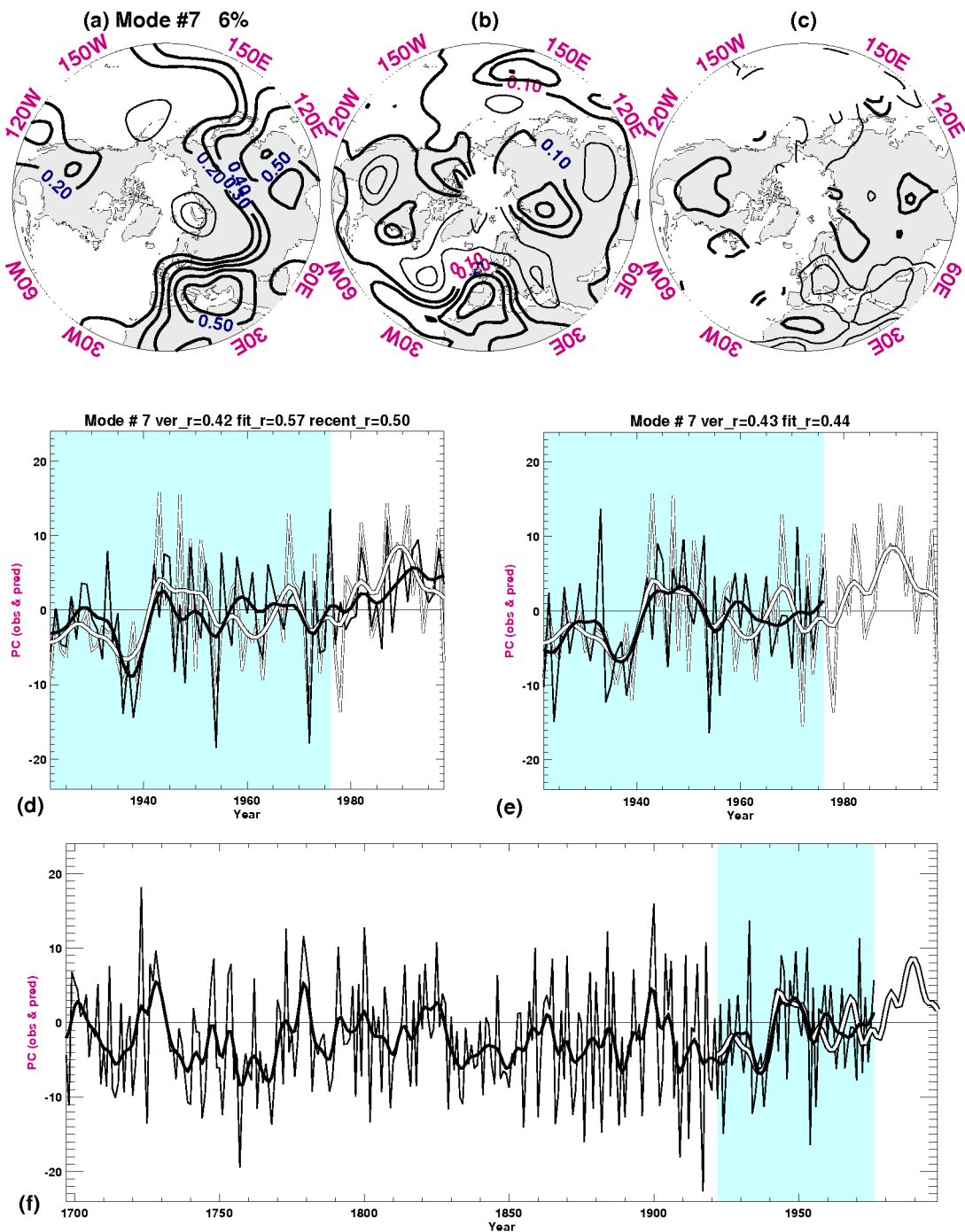


**Figure 18** As Figure 13, but for the seventh rotated PC of the SLP data.

circulation. Our initial attempts to exploit this potential have been disappointing. Sensitivity tests using actual observed (instrumental) temperature predictors perform only a little better. This indicates that it is the relative weakness of the relationship between large-scale atmospheric circulation patterns and land air temperature that is the limiting factor, especially for the short overlap period (55 years) used in this study for calibration and verification. Sensitivity tests using different calibration and verification periods and other aspects of the regression procedure (such as number of potential predictors offered, choice of entry/exit threshold) result in low confidence for the circulation reconstructions attempted.

Uncertainty ranges have not been included with the reconstructions due to their preliminary nature, and also because they can only be estimated on the basis of the instrumental period. Due to the indirect link between tree-ring density and

atmospheric circulation (i.e., the link is via the land temperature), uncertainties estimated over the instrumental period may under-represent the real range of possibilities. This is because there are two assumptions that are made when reconstructing past circulation variations. In addition to assuming that the relationship between each proxy series and its local climate is stationary, it must also be assumed that the response of surface climate to atmospheric circulation variations is stationary. These assumptions must always be made, but the reliability of reconstructions can be improved by extending the period of overlap with instrumental data (in this case, by widespread updating of tree-ring chronologies to the present), and by including the wealth of other summer-responsive proxy records that are available. Evidence is presented here, for example, that suggests that moisture- or drought-sensitive proxy records would improve the reconstruction of some circulation patterns.

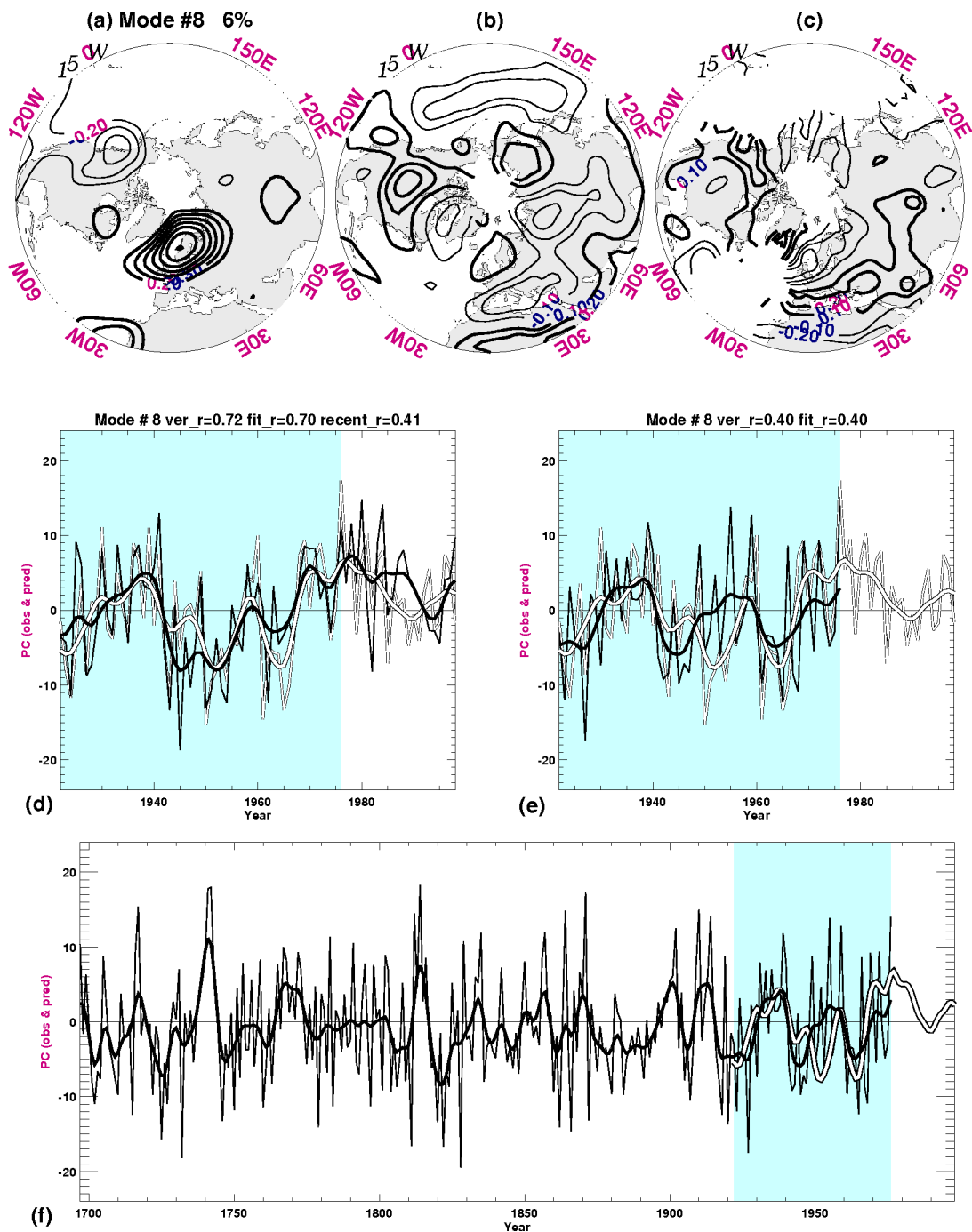


Figure 19 As Figure 13, but for the eighth rotated PC of the SLP data.

## Acknowledgements

This study and the assembly of the tree-ring data set were supported by the Commission of the European Communities (ADVANCE-10K, ENV4-CT95-0127), the UK Natural Environment Research Council (GR3/12107) and the US Department of Energy (DE-FG02-98ER62601). Data sets were kindly provided by Mike Hulme (University of East Anglia) and the Hadley Centre for Climate Prediction and Research (UK Meteorological Office).

## References

- Barnston, A.G. and Livezey, R.E. 1987: Classification, seasonality, and persistence of low-frequency atmospheric circulation patterns. *Monthly Weather Review*, 115, 1083–1126.
- Basnett, T.A. and Parker, D.E. 1997: *Development of the Global Mean Sea Level Pressure data set GMSLP2*. Climate Research Technical Note 79, Hadley Centre, Meteorological Office, Bracknell, UK, 16 pp.
- Briffa, K.R., Jones, P.D., Schweingruber, F.H., Karlén, W. and Shiyatov, S.G. 1996: Tree-ring variables as proxy-indicators: problems with low-frequency signals. In Jones, P.D., Bradley, R.S. and Jouzel, J., editors, *Climatic variations and forcing mechanisms of the last 2000 years*, NATO ASI Series 141, Berlin: Springer, 9–41.
- Briffa, K.R., Jones, P.D., Schweingruber, F.H. and Osborn, T.J. 1998a: Influence of volcanic eruptions on Northern Hemisphere summer temperature over the past 600 years. *Nature* 393, 450–55.
- Briffa, K.R., Jones, P.D., Wigley, T.M.L., Pilcher, J.R. and Baillie, M.G.L. 1986: Climate reconstruction from tree rings. Part 2, Spatial reconstruction of summer mean sea-level pressure patterns over Great Britain. *Journal of Climatology* 6, 1–15.
- Briffa, K.R., Osborn, T.J., Schweingruber, F.H., Harris, I.C., Jones, P.D., Shiyatov, S.G. and Vaganov, E.A. 2001: Low-frequency

- temperature variations from a northern tree ring density network. *Journal of Geophysical Research* 106, 2929–41.
- Briffa, K.R., Schweingruber, F.H., Jones, P.D., Osborn, T.J., Shiyatov, S.G. and Vaganov, E.A.** 1998b: Reduced sensitivity of recent tree-growth to temperature at high northern latitudes. *Nature* 391, 678–82.
- Cook, E.R., Briffa, K.R. and Jones, P.D.** 1994: Spatial regression methods in dendroclimatology – a review and comparison of two techniques. *International Journal of Climatology* 14, 379–402.
- Cook, E.R., Briffa, K.R., Meko, D.M., Graybill, D.S. and Funkhouser, G.** 1995: The 'segment length curse' in long tree-ring chronology development for paleoclimatic studies. *The Holocene* 5, 229–37.
- Cook, E.R., D'Arrigo, R.D. and Briffa, K.R.** 1998: A reconstruction of the North Atlantic Oscillation using tree-ring chronologies from North America and Europe. *The Holocene* 8, 9–17.
- Cook, E.R., D'Arrigo, R.D. and Mann, M.E.** 2002: A well-verified, multiproxy reconstruction of the winter North Atlantic Oscillation index since AD 1400. *Journal of Climate* 15, 1754–64.
- Cook, E.R., Meko, D.M., Stahle, D.W. and Cleaveland, M.K.** 1999: Drought reconstructions for the continental United States. *Journal of Climate* 12, 1145–62.
- Draper, N.R. and Smith, H.** 1981: *Applied regression analysis*. New York: John Wiley, 709 pp.
- Fritts, H.C.** 1976: *Tree rings and climate*, New York and London: Academic Press, 567 pp.
- 1991: *Reconstructing large-scale climatic patterns from tree-ring data: a diagnostic analysis* Tucson, AZ: University of Arizona Press, 286 pp.
- Fritts, H.C., Blasing T.J., Hayden, B.P. and Kutzbach, J.E.** 1971: Multivariate techniques for specifying tree-growth and climate relationships and for reconstructing anomalies in paleoclimate. *Journal of Applied Meteorology* 10, 845–64.
- Hirschboeck, K.K., Ni, F., Wood, M.L. and Woodhouse, C.A.** 1996: Synoptic dendroclimatology: overview and outlook. In Dean, J.S., Meko, D.M. and Swetnam, T.W., editors, *Tree rings, environment, and humanity*, Tucson, AZ: Radiocarbon, 205–23.
- Hulme, M.** 1994: Validation of large-scale precipitation fields in General Circulation Models. In Desbois, M. and Desalmand, F., editors, *Global precipitation and climate change*, NATO ASI Series, Berlin: Springer, 387–406.
- Jones, P.D.** 1987: The early twentieth century Arctic high – fact or fiction? *Climate Dynamics* 1, 63–75.
- 1994: Hemispheric surface air temperature variations: a reanalysis and an update to 1993. *Journal of Climate* 7, 1794–802.
- Jones, P.D., New, M., Parker, D.E., Martin, S. and Rigor, I.G.** 1999: Surface air temperature and its variations over the last 150 years. *Reviews of Geophysics* 37, 173–99.
- Kaiser, H.F.** 1958: The varimax criterion for analytic rotation in factor analysis. *Psychometrika* 23, 187–200.
- Kelly, P.M., Jones, P.D. and Jia, P.Q.** 1999: Spatial patterns of variability in the global surface air temperature data set. *Journal of Geophysical Research* 104, 24237–56.
- Osborn, T.J., Briffa, K.R. and Jones, P.D.** 1997: Adjusting variance for sample-size in tree-ring chronologies and other regional-mean timeseries. *Dendrochronologia* 15, 89–99.
- Osborn, T.J., Briffa, K.R., Schweingruber, F.H. and Jones, P.D.** 2002: Annually resolved patterns of summer temperatures over the Northern Hemisphere since AD 1400 from a tree-ring-density network. (In preparation)
- Osborn, T.J., Conway, D., Hulme, M., Gregory, J.M. and Jones, P.D.** 1999: Air flow influences on local climate: observed and simulated mean relationships for the United Kingdom. *Climate Research* 13, 173–91.
- Parker, D.E., Folland, C.K. and Jackson, M.** 1995: Marine surface temperature: observed variations and data requirements. *Climate Change* 31, 559–600.
- Rogers, J.C.** 1990: Patterns of low-frequency monthly sea level pressure variability (1899–1986) and associated wave cyclone frequencies. *Journal of Climate* 3, 1364–79.
- Salinger, M.J., Palmer, J.G., Jones, P.D. and Briffa, K.R.** 1994: Reconstruction of New Zealand climate indices back to AD 1731 using dendroclimatic techniques: some preliminary results. *International Journal of Climatology* 14, 1135–49.
- Schweingruber, F.H. and Briffa, K.R.** 1996: Tree-ring density networks for climate reconstruction. In Jones, P.D., Bradley, R.S. and Jouzel, J., editors, *Climatic variations and forcing mechanisms of the last 2000 years*, NATO ASI Series 141, Berlin: Springer, 43–66.
- Stahle, D.W. and 14 others** 1998: Experimental dendroclimatic reconstruction of the Southern Oscillation. *Bulletin of the American Meteorological Society* 79, 2137–52.
- Villalba, R., Cook, E.R., D'Arrigo, R.D., Jacoby, G.C., Jones, P.D., Salinger, M.J. and Palmer, J.** 1997: Sea-level pressure variability around Antarctica since AD 1750 inferred from subantarctic tree-ring records. *Climate Dynamics* 13, 375–90.
- Wallace, J. and Gutzler, D.** 1981: Teleconnections in the geopotential height field during the Northern Hemisphere winter. *Monthly Weather Review* 109, 784–812.